ICARUS **132,** 321–343 (1998)
ARTICLE NO. IS985897

Ribbon Terrain Formation, Southwestern Fortuna Tessera, Venus: Implications for Lithosphere Evolution

Vicki L. Hansen and James J. Willis

Department of Geological Sciences, Southern Methodist University, Dallas, Texas 75275-0395
E-mail: vhansen@mail.smu.edu

Received March 31, 1997; revised December 4, 1997

The term tessera has been used to describe regions of deformed venusian crust exhibiting two or more intersecting sets of structural elements; however, tessera includes terrains formed by a variety of spatially and temporally discrete tectonic processes. Tessera fabric characterizes highland plateau structure, and thus understanding the nature of this deformation is critical to understanding the mode of highland plateau formation. Many tessera fabrics include ribbons, folds, and late graben. In this paper, we refine the geometry of ribbons through geologic mapping and radargrammetric analysis of type ribbon structures at southwestern Fortuna Tessera; we extend our findings to ribbon fabrics at Thetis Regio. Any model of ribbon formation must account for the following constraints on ribbon geometry. (a) Ribbon-forming lineaments exhibit sharp contrasts relative to adjacent materials. (b) Ribbon-bounding lineaments form a distinct pattern alternating between radar-dark and radar-bright, which represent trough walls oriented away from and toward the satellite, respectively. (c) Ribbons form long, narrow troughs that alternate with parallel, narrow ridges; ridges and troughs display extreme length : width aspect ratios. (d) Trough walls are near vertical. (e) Troughs are shallow with consistent shallow depth along individual troughs and in adjacent troughs. (f) In some cases (e.g., southwest Fortuna Tessera) trough walls are parallel and matched and would exhibit a close fit if the trough was closed; in these cases trough walls merge laterally forming V-shaped terminations. Trough floors are smooth and flat, lacking small-scale interior lineaments. (g) In other cases (e.g., Thetis Regio) ribbons display (a)–(d), but trough walls are defined by a series of subparallel lineaments including local interior lineaments, and trough floors ramp up to join trough walls displaying parallel rather than V-shaped terminations. Trough walls would not display a close fit if closed.

We propose two member types of ribbons, tensile-fracture ribbons and shear-fracture ribbons. Tensile-fracture ribbons display features (a)–(f) and formed by the opening of tensile fractures of a thin brittle layer above a ductile substrate. They require a near fracture-free shallow crust and very shallow depth to the brittle–ductile transition (BDT) (<1 km). Shear-fracture ribbons display features (a)–(d) and (g) formed under near-surface transitional-tensile failure conditions or due to reactivation of steeply oriented preexisting fractures resulting in steep-sided graben. Formation of tensile-fracture ribbons would be favored with a sharp BDT at very shallow depth, whereas a broader and somewhat deeper BDT would favor formation of shear-fracture ribbons. In both cases, the thickness of the strong upper layer is quite thin (<1–2 km), and ribbon structures likely formed prior to long-wavelength folds, which require a greater effective elastic thickness and a deeper depth of support (~6 km).

The presence of ribbon structures within highland plateaus favors an upwelling model for highland plateau formation, in which crustal thickening results from magmatic underplating related to a mantle upwelling or mantle plume. In order for the plume to be able to anneal mechanically the crust as required by ribbon formation, the lithosphere would likely have to be quite thin. These implications are consistent with highland plateaus as an ancient signature of mantle plumes on thin lithosphere, whereas volcanic rises, which are presently thermally supported, reflect thick lithosphere. Phoebe Regio represents a transitional lithospheric thickness. © 1998 Academic Press

Key Words: **boudins; geological processes; radar; Venus; Venus, surface.**

INTRODUCTION

The term tessera (pl. tesserae; Latin for tile) has been used to describe regions of deformed venusian crust exhibiting two or more intersecting sets of structural elements, high cm- to m-scale surface roughness and high relief relative to surrounding volcanic plains (e.g., Barsukov *et al.* 1985, 1986, Basilevsky *et al.* 1986, Sukhanov 1986, 1987, Bindschadler *et al.* 1990, 1992a, 1992b, Bindschadler and Head 1991, Solomon *et al.* 1991, 1992, Ivanov and Basilevsky 1993). Tessera has become a catch-all term for terrains exhibiting apparently complex deformation. However, tesserae record a variety of spatially and temporally discrete tectonic deformations representing different tectonic processes—the origin of which must be examined individually (Hansen and Willis 1996). By analogy, peas and carrots are

[1] Current address: Department of Geology, University of Southwestern Louisiana/Universite des Acadiens, Lafayette, LA 70504.

0019-1035/98 $25.00

both classified as vegetables, yet they represent markedly different products formed by different processes in different environments; to understand them we must study each individually. In this paper, we examine the origin of ribbon terrain, a tessera fabric exposed in venusian highland plateaus (Hansen and Willis 1996).

The term tessera comes from the tile-like patterns revealed by Soviet Venera radar imagery (Barsukov *et al.* 1985). Although general patterns were visible, the low-image resolution relative to individual structural fabrics could not allow adequate characterization of the structural styles and strain histories. Magellan SAR (Synthetic Aperture Radar) imagery provides much higher resolution for structural analysis, and efforts are being made to describe and interpret the structural forms and tectonic evolution of various types of deformed crust called tesserae (e.g., Bindschadler *et al.* 1992a, Hansen and Willis 1996).

In this paper, we focus our attention on a particular structural fabric, common to certain tessera types, termed ''ribbons.'' Mechanisms of ribbon formation and the temporal relations of ribbons and spatially associated structures provide fundamental constraints for models of tessera formation and highland plateau evolution. We elaborate on our prior reconnaissance treatment of ribbons (Hansen and Willis 1996). Herein we (1) refine the geometric description of ribbons resulting from detailed mapping and radargrammetric analysis in southwestern Fortuna Tessera; (2) discuss models for ribbon formation and temporal relations between ribbons and folds; (3) present models for tensile-fracture ribbons and shear-fracture ribbon, and (4) outline implications of ribbon formation for highland plateau formation and lithosphere evolution.

GENERAL GEOLOGY OF SOUTHWESTERN FORTUNA TESSERA

The Soviet Venera 15 and 16 probes imaged Ishtar Terra, Venus, providing radar images that revealed an elevated region of volcanic plains, Lakshmi Planum, bordered by high mountain ranges, including Maxwell Montes, Venus' highest at 11 km above mean planetary radius (MPR). East and south of Maxwell Montes, Fortuna Tessera comprises a region that lies ~4 km above MPR and is characterized by apparently complex deformation, originally termed parquet terrain and later tessera terrain (Fig. 1a) (Barsukov *et al.* 1985, 1986, Basilevsky *et al.* 1986, Sukhanov 1986, 1987, Bindschadler *et al.* 1990).

Southwestern Fortuna Tessera is an excellent region to study ribbon geometry and strain history because (a) the area hosts ribbons and folds in near-orthogonal relation, allowing detailed analysis of ribbons as they cross fold crests and troughs; (b) volcanic lava flows locally embay synform fold valleys and ribbon troughs, providing a cross section of ribbons, and (c) the radar look direction is nearly orthogonal to ribbons, allowing application of radargrammetric techniques to constrain the three-dimensional ribbon geometry.

Magellan SAR imagery of Fortuna Tessera allows for detailed structural analysis of Fortuna tectonic fabrics. Full-resolution (FMIDR) left-looking (radar illumination from the west) images are available for southwestern Fortuna Tessera. We selected a 165 × 225 km area in which we examined ribbon geometry in detail (Fig. 1). The region is the type location for ribbon structures (Hansen and Willis 1996). North-trending ribbons intersect with east-trending warps or gentle folds. Flood-type lava flows, derived from a large caldera complex to the west, locally flood the structural (and topographic) lows.

Folds. Broad ridges and valleys trend east subparallel to the radar look direction. We follow previous interpretations that the ridges represent folds based on the gradational nature of radar brightness across the ridge crests (e.g., Ford *et al.* 1993). Local flooding of synform valleys by lava flows confirms their low topography relative to adjacent antiform ridges. We interpret the folds as gentle given a wavelength of ~7 to 20 km and broadly similar altimetry across the region. This interpretation is supported by radargrammetric calculations that indicate fold limb dip of ~20° and thus interlimb angles of ~140° (see below).

Ribbons. Ribbons comprise a fabric of alternating, parallel, closely spaced, sharp, radar-dark and radar-bright lineaments. Individual lineaments exhibit sharp, not gradational, brightness contrast with adjacent materials. Lineaments show a distinct dark–bright pairing defining a system of slopes that together define a series of alternating troughs and ridges that trend north (Fig. 1). The troughs are bounded to the west by radar-dark slopes and to the east by radar-bright slopes, with ridges adjacent; local embayments by volcanic lava flows confirm the low topography. Troughs range from 0.6–3 km wide with a mode of 1.2 km (Table I), and range in length up to 170 km (Pritchard *et al.* 1997). Ridges range in width from 0.4–3.6 km with a mode of 1.2 km (Table I). Ridges are longer than troughs because a ridge can continue as a trough ends on one side (Fig. 2). (Hansen and Willis 1996, p. 302 cited a trough width of 2–7 km, but incorrectly used the average width of ridge–trough pairs.) Thus, the troughs exhibit a high length-to-width aspect ratio of 50–100 : 1; this extreme aspect ratio is the root of the term ''ribbon'' or ''ribbon structure.'' Ribbon troughs typically cut at a high angle across the aforementioned gentle, east-trending, folds (Fig. 1). The troughs appear sinuous, yet most changes of trough position correlate to location relative to their position on the folds; the trough-bounding lineaments—the trough walls—are consistently shifted westward at antiform crests relative to their position in adjacent synform valleys, independent of

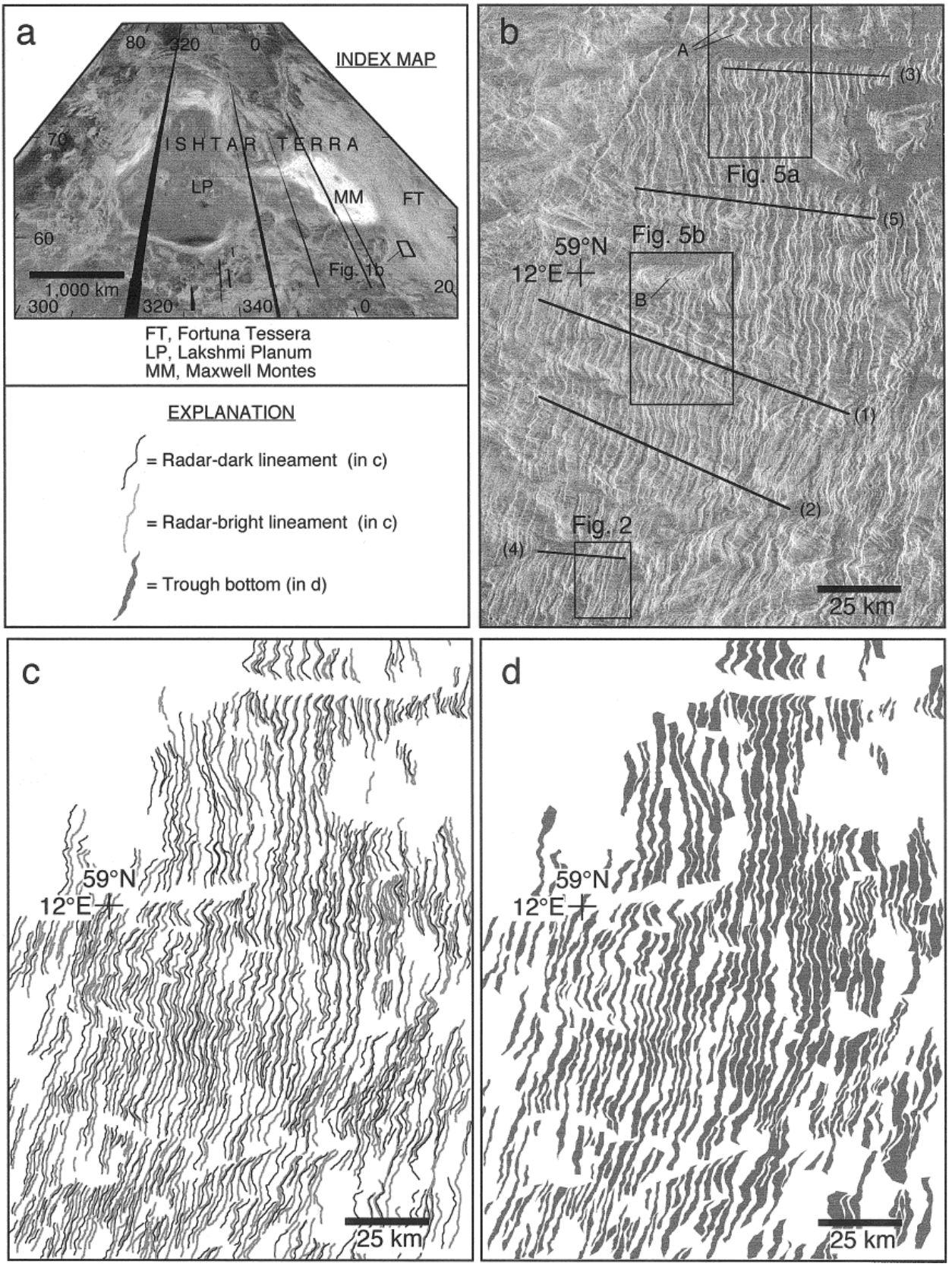

FIG. 1. Ribbon structures at southwestern Fortuna Tessera. (a) Location map with location of constraint (b) shown by box; explanation for maps of constraints (c) and (d). (b) Radar base image extracted from F-MIDRP.60N016;1 and reprojected in sinusoidal format. Satellite is to the west or left. Boxes show the locations of Figs. 2, 5a, and 5b; locations A and B discussed in text; lines labeled with numbers in brackets show locations of ribbon transects in Table I; transects 1 and 2 are from Pritchard *et al.* (1997). (c) Map delineating radar-dark and radar-bright lineaments that represent slopes tilted away from and toward the satellite, respectively. East-trending white areas are lava flow flooded synformal valleys. (d) Map delineating the troughs located between paired radar-dark and radar-bright lineaments.

TABLE I
Fortuna Ribbons (in km)

	Mean		Mode		Minimum		Maximum		Elongation (%)
	Ridges	Troughs	Ridges	Troughs	Ridges	Troughs	Ridges	Troughs	
Transect 1 (98.2 km)	1.6	1.3	1.2	1.2	0.6	0.6	3.6	2.4	76
2 (89.9 km)	2.5	1.4	2.4	1.2	1.0	0.6	4.7	3.0	58
3 (54.4 km)	1.2	0.9	0.8	0.8	0.4	0.4	3.2	2.0	74
4 (26.0 km)	1.0	0.8	1.0	0.4	0.4	0.4	2.8	2.0	82
5 (67.6 km)	7.0	1.5	1.6	1.2	0.4	0.4	9.4	3.6	84
Transects combined	2.7	1.2	1.2	1.2	0.4	0.4	9.4	3.6	

Note. Transect locations are shown in Fig. 1b; transects 1 and 2 from Pritchard *et al*. (1997).

ribbon or fold trend. This apparent westward bending of lineaments across antiform crests results from radar foreshortening, a data artifact common at high latitudes due to the relatively low incidence angle (Plaut 1993a). Additional evidence of radar artifacts occurs at the embayments of lava flows into ribbon troughs, whereby radar-bright west-facing trough walls ''overlay'' part of the flooded trough valley, locally obscuring the real embayment shoreline.

Although trough width varies somewhat along trend, paired trough walls—lineaments that mark opposite sides of the same trough—remain essentially parallel and matched along their length even as they track across topographic fold crests and valleys (Fig. 1). For example, if a lineament deviates westward then back east, its counterpart on the opposite side of the trough does the same. No correlation exists between trough widening and fold crests, which might be expected if ribbon troughs represented classic graben defined by normal faults that cut folds (Fig.

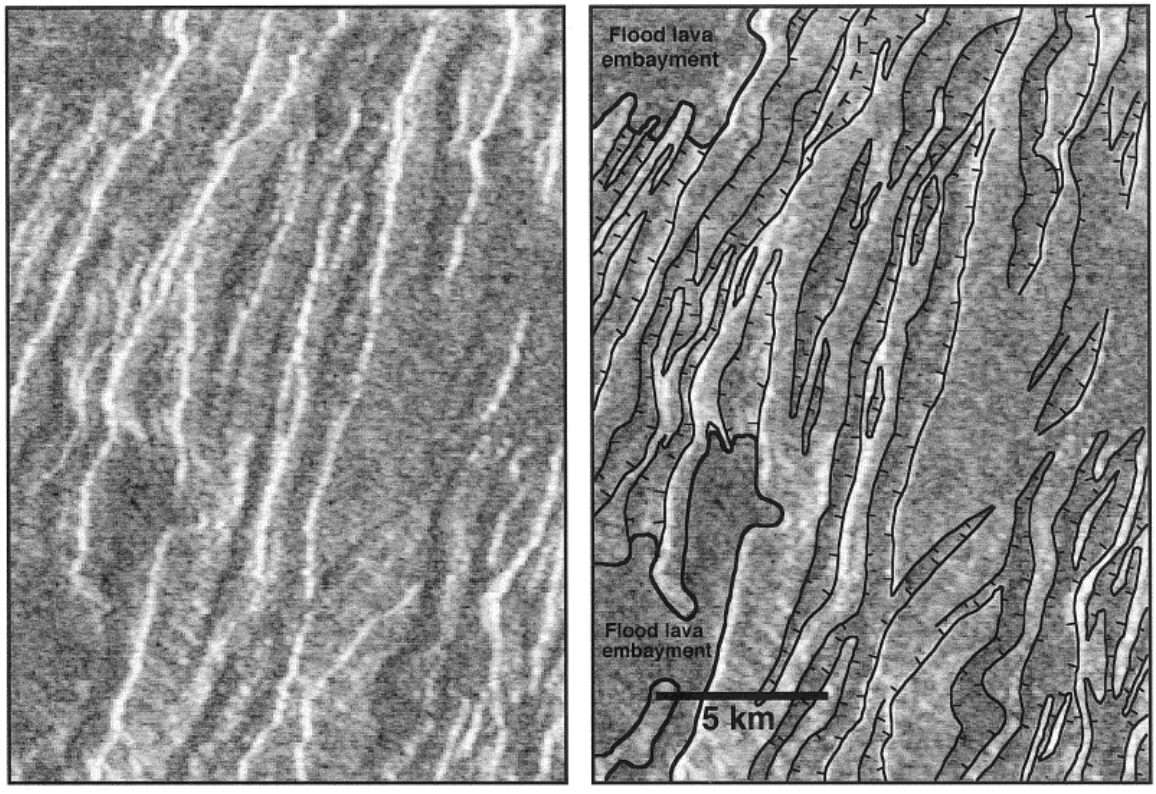

FIG. 2. SAR image and map of ribbon terminations at southwestern Fortuna Tessera (location shown in Fig. 1b); hatched lines delineate trough walls with ticks on the trough side; thick lines mark extent of lava flow embayments.

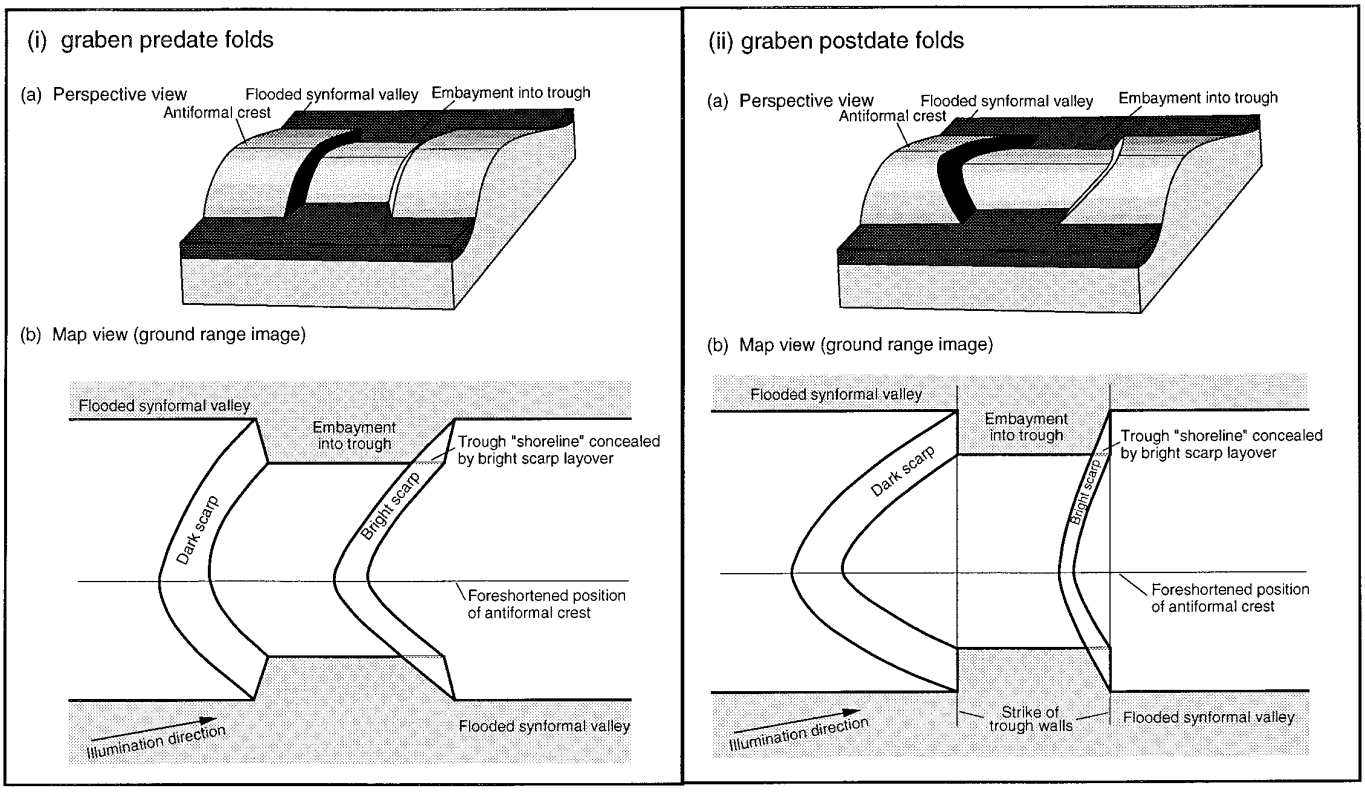

FIG. 3. Block diagrams (a) and map view (b) illustrating geometric relations of ribbons if resulted from normal-fault graben that predated folds (i) or postdated (ii) folds.

3) (e.g., Baldwin 1971, McGill 1971, Golombek 1979). This observation is important because it indicates that the ribbon troughs cannot be the result of graben that formed after the folds. Instead, paired trough walls are deflected equally at fold crests due to foreshortening, indicating that the trough walls formed before the folds, the walls are vertical, or both (Fig. 3). In contrast to the paired trough walls, the walls that bound either side of a ridge (ridge walls) are not matched with one another, although they maintain the same regional trend. In addition, trough wall lineaments do not terminate singly as would be expected for graben walls in which fault scarps remain apart and trough floors ramp up (e.g., McGill and Stromquist 1979); instead, walls on either side of a trough merge laterally with one another into V-shaped terminations (Fig. 2). Although the orientation of individual lineaments may shift due to a trough merging or bifurcating, even in these situations walls on either side of a trough are paired and merge laterally. Trough bottoms appear flat, smooth, and notably devoid of interior lineaments as evidenced by lava embayment relations discussed below.

Radargrammetric Constraints on Ribbon Dip and Depth

The three-dimensional geometry of ribbons constrains interpretations of their structural style and origin. The altimeter footprint of approximately 21 by 8 km at >60° latitude (Plaut 1993b) cannot profile the ribbon structures. However, radargrammetric calculations provide a means for determining detailed vertical relief and therefore ribbon-trough depth and trough wall dip. Our calculations will actually be dealing with current slopes, as opposed to original slopes. But erosion and mass-wasting, the major factors that might modify slopes on Venus, should result in a decrease in slope over time, and therefore our calculations provide *minimum* estimates of the original slope angles.

Locations of image pixels (or resolution cells), which are converted to planetary latitude and longitude, are derived from two factors (Plaut 1993b) (1) across-track distance or range—the distance from antenna to imaged features—is determined by the time delay of an echo pulse, whereas (2) along-track position is based on the expected Doppler shift of a returned pulse from a given terrain. The transformation of radar echoes to image pixels is based on assumptions of the long-wavelength shape (hundreds of kilometers) of the imaged surface. Smaller-scale variants to this assumed shape, particularly changes in local topography, however, affect the location of pixels, resulting in geometric distortions of imaged features. Because high areas are closer to the spacecraft than surrounding areas, they return

an echo sooner than adjacent low areas; therefore, high areas are shifted toward the spacecraft in the look direction in the processed image. Low areas take longer to return echoes, and therefore they are shifted in the look direction away from the spacecraft. These shifts in the processed image, high features toward the radar and low features away from the radar, are termed foreshortening and elongation, respectively (Plaut 1993a). Layover represents extreme foreshortening, whereby an echo pulse from a mountain top apparently overlays or is superimposed on the valley bottom, and possibly onto the next ridge flank. Thus, radar foreshortening and elongation distortions preserve information regarding the vertical dimension. Heights are typically determined by comparing distortions of the same feature on stereoscopic radar images, two images with different incident angles and with either same-side or opposite-side look directions (e.g., Plaut 1993b, Conners 1995). Unfortunately, the study area of Fig. 1 has only been imaged by cycle-1 Magellan data. In certain situations a single radar image can be used to determine heights (Weitz 1993). Key factors for such analysis include presence of opposite-dipping slopes and assumption of symmetry (i.e., same dip angle for both slopes). Equations for determining feature heights from single radar images are case specific. For example, the equations used by Weitz (1993) are not applicable if radar layover is present, as is the case with the radar-bright, ribbon-bounding lineaments in southwestern Fortuna Tessera.

We define new equations for the Fortuna ribbon structures. We assume symmetry of opposite trough walls, a justified assumption because the near parallelism and matching of paired trough walls implies symmetry.

Southwestern Fortuna Tessera represents an excellent area for radargrammetric analysis because (1) trough walls track across fold crests while maintaining parallelism, which implies similar dip relations or symmetry, (2) folds and ribbons occur in a near-orthogonal relation, (3) radar-illumination direction nearly parallels the trend of the fold crests and occurs nearly orthogonal to the ribbons, simplifying radargrammetric calculations, and (4) several synform valleys and ribbon troughs are embayed by volcanic flood lava, which we assume as a horizontal base level for height determinations, thus, embayment patterns provide clues to the detailed topography and therefore the three-dimensional character of the ribbon and fold structures.

Figure 4 presents simplified, diagrammatic illustrations of relations of ribbons observed at southwestern Fortuna Tessera, specifically opposite-dipping paired slopes with flat-ridge tops and trough bottom, and layover of the radar-bright trough bounding wall, simulating the relations observed at southwestern Fortuna Tessera. More detailed relations are discussed later. We use the observed layover of the radar-bright scarps as the initial control for derivations (the presence or absence of layover requires the use of different equations; see Weitz 1993 and Willis 1997). The layover indicates simply that the slope angle of the trough walls is greater than the incidence angle (θ_i). Two possible variations exist, dependent upon the relation between slope angle (ϕ_a) and the complement of incidence angle ($90 - \theta_i$). If the slope angle is greater than the complement of incidence angle (i.e., if $\phi_a > 90 - \theta_i$), then the radar-dark slope will be shadowed (Fig. 4a), otherwise that slope will not be in radar shadow (Fig. 4b).

The following equations are derived for the case where $\phi_a > 90 - \theta_i$. From Fig. 4a, and using the radar-dark, shadowed lineament,

$$s_{ds} = g_{ds} \sin \theta_i \tag{1a}$$

and

$$s_{ds} = h_t / \cos \theta_i, \tag{1b}$$

where s_{ds} is the slant range distance of the dark scarp parallel to the illumination direction, g_{ds} is the ground range distance or width of the dark scarp as measured parallel to the illumination direction, θ_i is the incidence angle, and h_t is the vertical trough height. Solving Eqs. (1a) and (1b) simultaneously for h_t gives

$$h_t = g_{ds} \sin \theta_i \cos \theta_i. \tag{2}$$

An important aspect of this calculation is that the trough depth can be determined independent of the dip of the trough walls. A slope with an angle greater than the complement of incidence angle will be shadowed, and thus incidence angle and trough height are the only controls on ground range slope width. In that incidence angle is known for given latitudes (Plaut 1993a) and ground range slope width parallel to the illumination direction can be measured from the radar image, the slope height can be determined.

Both the radar-dark and radar-bright slope widths can be used to determine slope angles, assuming symmetry, a plausible assumption as discussed earlier. From Fig. 4a,

$$\tan \theta_i = h_t / (g_{bs} + zz) \tag{3a}$$

and

$$\tan \phi_a = h_t / zz, \tag{3b}$$

where g_{bs} is the ground range distance or width of the bright scarp as measured parallel to the illumination direction, and zz is the true horizontal width of the bright scarp parallel to the illumination direction. Solving both equa-

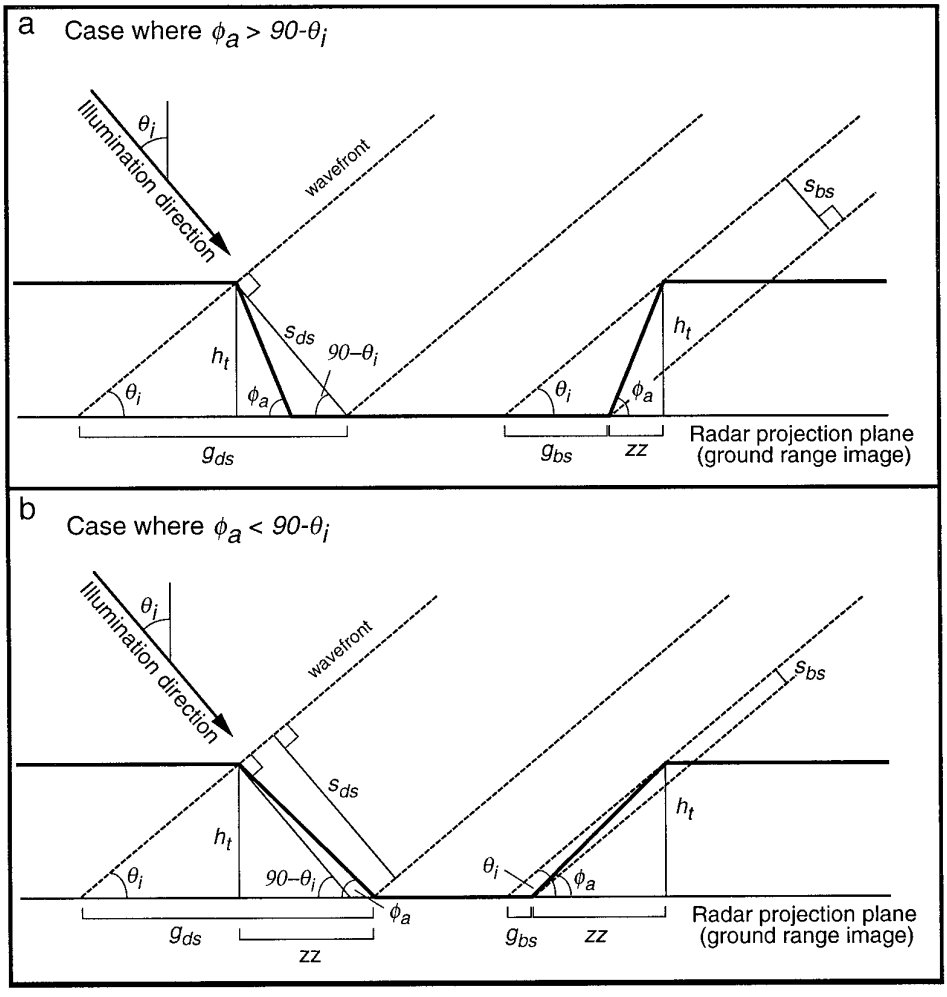

FIG. 4. Diagrammatic radargrammetric relations of paired, symmetric, opposite-dipping slopes relative to the complement of incidence angle. (a) Relations if slope angle is greater than the complement of the incidence angle, indicating shadowing of radar-dark slope. (b) Relations if slope angle is less than the complement of the incidence angle. θ_i, incidence angle; s_{ds}, slant range distance of the shadowed radar-dark slope as measured parallel to the illumination direction; g_{ds}, ground range distance or width of the shadowed radar-dark slope measured parallel to illumination direction; s_{bs}, slant range distance of the radar-bright slope measured parallel to the illumination direction; g_{bs}, ground range distance or width of the radar-bright slope measured parallel to the illumination direction; zz, actual horizontal width of slopes measured parallel to the illumination direction; h_t, vertical height of the trough walls; ϕ_a, apparent slope angle of the trough walls measured parallel to the illumination direction. Note that the ratio between g_{bs} and g_{ds} changes depending upon dip angle.

tions simultaneously to eliminate the unknown zz term yields

$$h_t/\tan\theta_i - g_{bs} = h_t/\tan\phi_a. \quad (4)$$

Replacing $h_t = g_{ds} \sin\theta_i \cos\theta_i$ from Eq. (2) and solving for slope angle ϕ_a gives

$$\phi_a = \text{atn}\,[(g_{ds}\sin\theta_i\cos\theta_i)/(g_{ds}\cos^2\theta_i - g_{bs})]. \quad (5)$$

The following equations are derived for the case where slope angle ϕ_a is less than the complement of incidence angle $90 - \theta_i$, thus the dark scarp is not a shadow effect. From Fig. 4b, and using the radar-dark lineament,

$$\tan\theta_i = h_t/(g_{ds} - zz), \quad (6a)$$

and using the bright scarp provides

$$\tan\theta_i = h_t/(g_{bs} + zz). \quad (6b)$$

Solving Eqs. (6a) and (6b) simultaneously yields

$$zz = (g_{ds} - g_{bs})/2, \quad (7)$$

and by substituting zz from Eq. (7) into either Eq. (6a) or (6b) gives

$$h_t = [(g_{ds} + g_{bs})/2] \tan \theta_i. \quad (8)$$

Unlike the case if $\phi_a > 90 - \theta_i$, where the dark slope is shadowed, determination of h_t in this case requires both slope width.

The slope angle can be now determined. From Fig. 4b,

$$\tan \phi_a = h_t/zz, \quad (9)$$

and substituting $zz = (g_{ds} - g_{bs})/2$ from Eq. (7) into Eq. (9) yields

$$\phi_a = \text{atn} [2 h_t/(g_{ds} - g_{bs})]. \quad (10)$$

Next, we discuss how to determine which suite of equations ((1)–(5) versus (6)–(10)) should be used to constrain trough depth (slope height) and trough wall dip (slope angle). The widths of the radar-dark and radar-bright slopes are dependent upon incidence angle, slope angle, and slope height. At a given locality, the incidence angle is constant and known, thus slope angle and slope height, both unknowns, control slope widths. Slope height influences both images radar-dark and radar-bright slope widths proportionally, but the slope angle determines the ratio between the ground range slope widths (see Fig. 4). Specifically, the width of the radar-dark slope is minimized and remains constant if that slope is in shadow (i.e., $\phi_a > 90 - \theta_i$). If $\phi_a < 90 - \theta_i$, the radar-dark slope is not in shadow, and the slope width increases with decreasing dip. The radar-bright slope width decreases with decreasing dip if that slope is laid over. Whether slope angle is less than or greater than the complement of incidence angle determines which set of equations to use. Because at a given incidence angle slope angle controls the ratio of apparent image radar-dark and radar-bright slope widths, we can modify the equations derived above to determine the ratio at the critical transition point, where $\phi_a = 90 - \theta_i$, and compare observed ratios from imagery to that determined critical ratio. Ratios greater than the critical ratio would indicate that $\phi_a > 90 - \theta_i$ and the first suite of equations (Eqs. (1)–(5)) should be used for radargrammetric calculations of slope angle and slope height. Ratios less than the critical ratio require $\phi_a < 90 - \theta_i$, and thus the second suite of equations (Eqs. (6)–(10)) should be used. As noted earlier, if the radar-bright scarp is not laid over, then yet another suite of equations is required (Weitz 1993, Willis 1997).

The critical ratio at the transition point of $\phi_a = 90 - \theta_i$ can be determined by substituting $90 - \theta_i$ for ϕ_a in Eq. (5), and solving for g_{bs}/g_{ds}. Starting with

$$\tan (90 - \theta_i) = (g_{ds} \sin \theta_i \cos \theta_i)/[g_{ds} \cos^2 \theta_i - g_{bs}], \quad (11a)$$

algebraic manipulation and rearrangement yields

$$g_{bs}/g_{ds} = \cos^2 \theta_i - (\sin \theta_i \cos \theta_i)/\tan (90 - \theta_i). \quad (11b)$$

The ratio at the transition point of $\phi_a = 90 - \theta_i$ can likewise be determined by substituting $90 - \theta_i$ for ϕ_a into Eq. (10). Starting with

$$\tan (90 - \theta_i) = 2 h_t/(g_{ds} - g_{bs}), \quad (12a)$$

and substituting $h_t = [(g_{ds} + g_{bs})/2] \tan \theta_i$ (Eq. (8)) yields

$$\tan (90 - \theta_i) = [(g_{ds} + g_{bs}) \tan \theta_i]/(g_{ds} - g_{bs}). \quad (12b)$$

Rearrangement gives

$$\begin{aligned} &(g_{ds} - g_{bs}) \tan (90 - \theta_i) = (g_{ds} + g_{bs}) \tan \theta_i, \\ &g_{ds} \tan (90 - \theta_i) - g_{bs} \tan (90 - \theta_i) = g_{ds} \tan \theta_i + g_{bs} \tan \theta_i, \\ &g_{bs}/g_{ds} = [\tan (90 - \theta_i) - \tan \theta_i]/[\tan (90 - \theta_i) + \tan \theta_i]. \end{aligned} \quad (12c)$$

Despite a different appearance, Eqs. (11b) and (12c) are mathematically identical, as established by a long, complex proof, or the reader may use simple numerical substitution to establish identity.

Slope widths were measured at 10 localities in southwestern Fortuna Tessera (Fig. 5). At each site, slope boundaries were mapped and three measurements of width parallel to the illumination direction between boundaries were made for each slope. Table II shows the mean slope widths and ratios at each site. The incidence angles at areas A and B are 28.5° and 28.7°, respectively (Plaut 1993a); thus, from Eqs. (11b) or (12c), the critical ratios are 0.55 and 0.54, respectively. In all cases, ratios at each locality exceed the critical ratio, indicating that $\phi_a > 90 - \theta_i$ ($\phi_a > 61.5°$ and 61.3°, respectively). We therefore use Eqs. (1)–(5) to determine slope height (or trough depth) and slope angle.

Trough depth can be determined from the width of the dark slope using Eq. (2). Table II presents these results. At area A, the mean dark-scarp width of 0.60 ± 0.08 km yields a mean depth of 0.25 ±0 .03 km; and at area B, the mean width of 0.54 ± 0.12 km yields a mean depth of 0.23 ± 0.05 km. As discussed earlier, given that $\phi_a > 90 - \theta_i$, the determined depths from Eq. (2) are independent of slope angle. These results point consistently to relatively shallow depths of the troughs throughout both areas and along individual troughs. For example, three depth calculations along a single trough in area B (localities 1, 2, and 4) range from 0.17–0.25 km. Furthermore, observations reveal remarkably consistent dark-slope widths

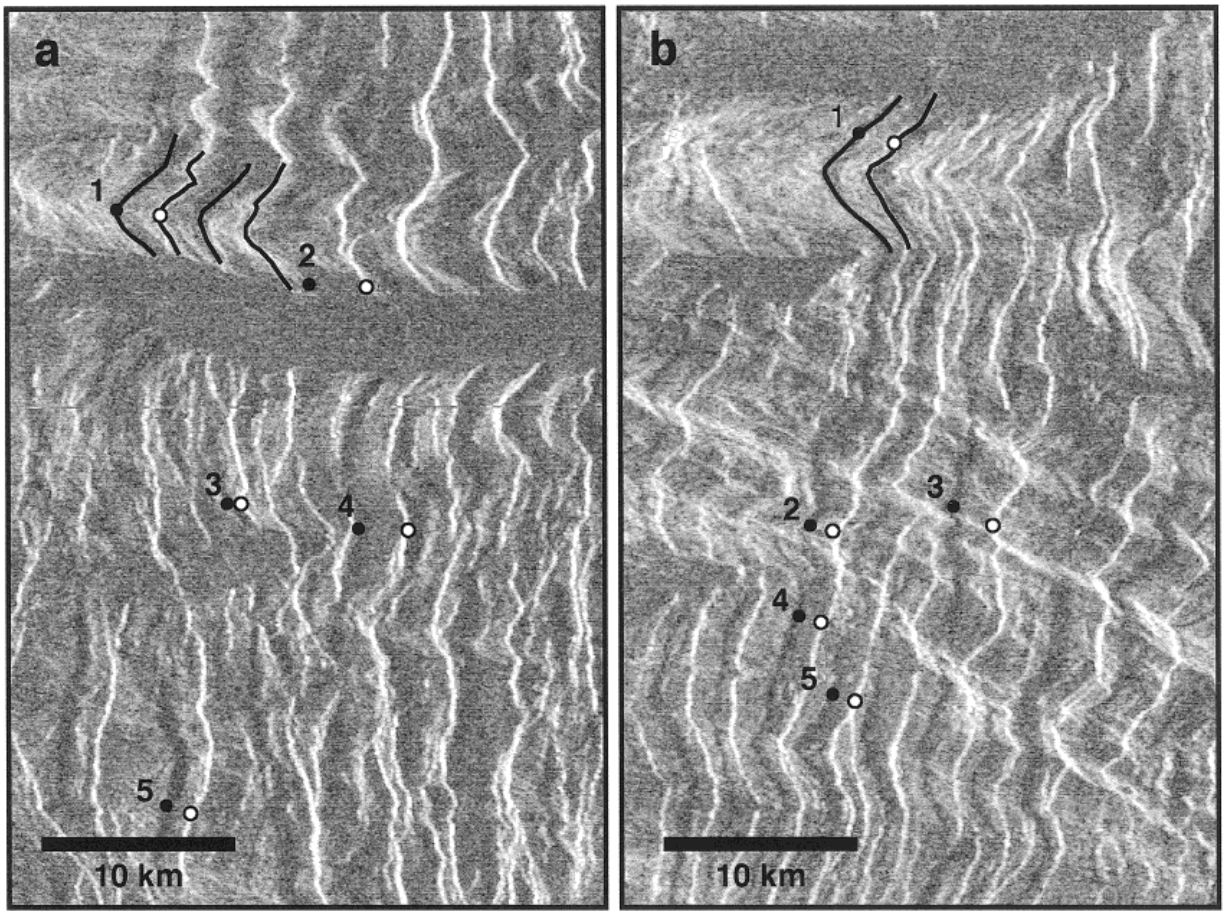

FIG. 5. SAR images of ribbon structures at areas A (a) and B (b). (a) centered at 59.5°N, 13°E; (b) centered by 58.9°N, 12.5°E (locations shown in Fig. 1b). Numbered dots correspond to paired slopes (closed circle for radar-dark slope; open circle for radar-bright slope) used for radargrammetric analysis of slope height and dip; results are shown in Table II. Bold lines correspond to paired lineament traces over fold crests used for radargrammetric calculations.

TABLE II
Relations between Slope Widths, Trough Height, and Slope Angle in Southwestern Fortuna Tessera

Locality	g_{ds} (km)	g_{bs} (km)	Ratio	h_t (km)	ϕ_a (deg)
		Area A			
1	0.68	0.41	0.60	0.29	68.0
2	0.58	0.39	0.67	0.24	76.6
3	0.49	0.36	0.73	0.21	84.9
4	0.68	0.47	0.69	0.29	79.0
5	0.56	0.40	0.71	0.23	82.1
Mean standard deviation	0.60 ± 0.08	0.41 ± 0.04	0.68 ± 0.05	0.25 ± 0.03	77.4 ± 6.5
		Area B			
1	0.41	0.31	0.76	0.17	88.2
2	0.60	0.42	0.70	0.25	80.6
3	0.72	0.48	0.67	0.30	76.3
4	0.47	0.37	0.79	0.20	92.4
5	0.50	0.38	0.76	0.21	88.7
Mean standard deviation	0.54 ± 0.12	0.40 ± 0.06	0.74 ± 0.05	0.23 ± 0.05	84.1 ± 6.6

throughout southwestern Fortuna Tessera, indicating consistent, shallow depths throughout the region.

Slope angles can be determined using Eq. (5). Results are shown in Table II. Mean slope angles for areas A and B are 77.4 ± 6.5° and 84.1 ± 6.6°, respectively. Because the dark scarps are better defined in area B than in area A (see Fig. 5), we are more confident of our calculations at area B. Furthermore, because our calculations determine present slope angles and because mass-wasting processes tend to reduce slope angles over time, our estimates are minimum estimates. Thus, results point to steep, nearly vertical slope angles, or near-vertical trough walls.

In addition to radargrammetric calculations using slope widths, we can also use the deflection of ribbon structures as they track across folds to derive certain constraints. First, we solve for the height of an antiform above embayment level. Using the radar-dark lineaments (Fig. 6), we determine that

$$\tan \theta_i = h_{af}/(g_x - z), \tag{13a}$$

where h_{af} is the antiform height above volcanic flood level, g_x is the distance in map view (parallel to radar illumination) of the deflected radar-dark lineament of the intersection between the upper part of the trough wall and fold (i.e., the western boundary of the radar-dark lineament) from its projected trend at embayment level to its position at the fold crest, and z is the true horizontal distance (i.e., without radar deflection) parallel to radar illumination of the lineament edge from its projected trend at embayment level to its position at the fold crest. The ground range distance g_x is measured from the radar image. Although the radar-dark lineaments represent the shadow of the steeply dipping, western trough walls, the deflections of those lineaments across fold axes are not a shadowing effect because the crestal position of the lineament relative to the valley position is not located parallel to the illumination direction. That is, high objects only shadow objects located parallel to the illumination direction. The western boundary, corresponding to the upper intersection between trough wall and fold, should be used rather than the eastern boundary, which is not the true lower intersection between trough wall and fold, but instead a shadow line. Both h_{af} and z remain unknowns, but by using the radar-bright lineament, we determine that

$$\tan \theta_i = h_{af}/(g_y + z), \tag{13b}$$

where g_y is the ground range distance parallel to radar illumination direction of the radar-bright lineament from its projected trend at embayment level to its position at the fold crest, again using the upper intersection between trough wall and fold, corresponding to the western boundary of the bright lineament trace on the image. Although in reality the upper intersection is east of the lower intersection, due to layover the upper trace appears west of the lower trace on the radar image (Fig. 6). Solving Eqs. (13a) and (13b) simultaneously yields

$$z = (g_x - g_y)/2. \tag{14}$$

Substituting z from Eq. (14) into either (13a) or (13b) results in

$$h_{af} = [(g_x + g_y)/2] \tan \theta_i. \tag{15}$$

Antiform heights above volcanic flood level were determined at two localities, A and B (Figs. 1 and 5). Radargrammetric calculations were completed for two troughs at locality A. For the western trough at A, g_x and g_y are 2.10 and 1.88 km, respectively, and θ_i is 28.5°, yielding an antiform height of 1.08 km above the lava surface. Trough lineament deflection values at the eastern trough at A are g_x = 2.33 km and g_y = 2.18 km, which yield an antiform height of 1.22 km. The position of the flood level approximately halfway between the antiform crest and the inferred synform trough indicates that these two height determinations are approximately half of the total height from synform trough to antiform crest. Flooding levels vary at other locales.

The deflected trough at locality B was imaged at a slightly different incidence angle, 28.7°, and exhibits g_x = 3.74 km and g_y = 3.6 km, yielding an antiform height of 1.94 km, which in this case is equal to the amplitude of the antiform because the measurement at B is from antiform crest to synform trough.

The deflection of radar-dark and radar-bright lineaments can also be used to constrain dip relations by assuming symmetry of the trough walls. The trough walls each form an upper and lower intersection lineation with the fold structure (Fig. 6). The dip determined is not necessarily the actual dip of the lineament slopes, but rather describes the planar geometry formed by an individual curved intersection lineation. For example, if the lineations represent graben-bounding normal faults formed before folding (Fig. 6i), then the slopes will dip in opposite directions toward the trough, but the intersection lineation of say the upper part of the radar-dark trough wall with the fold may describe a vertical plane (see ϕ_{itf} in Fig. 6). The same would be true if the lineaments represent vertical trough walls formed either prior to or after folding (Fig. 6). However, if the lineaments represent normal faults formed after folding, the slopes will be opposite dipping, and the intersection lineations between trough walls and the fold will describe the same dip angle (Figs. 3 and 6).

In our calculations, we determine g_x and g_y and thus the dip for the plane formed by the intersection the *upper* trough wall and the fold structure, because the *lower* trough

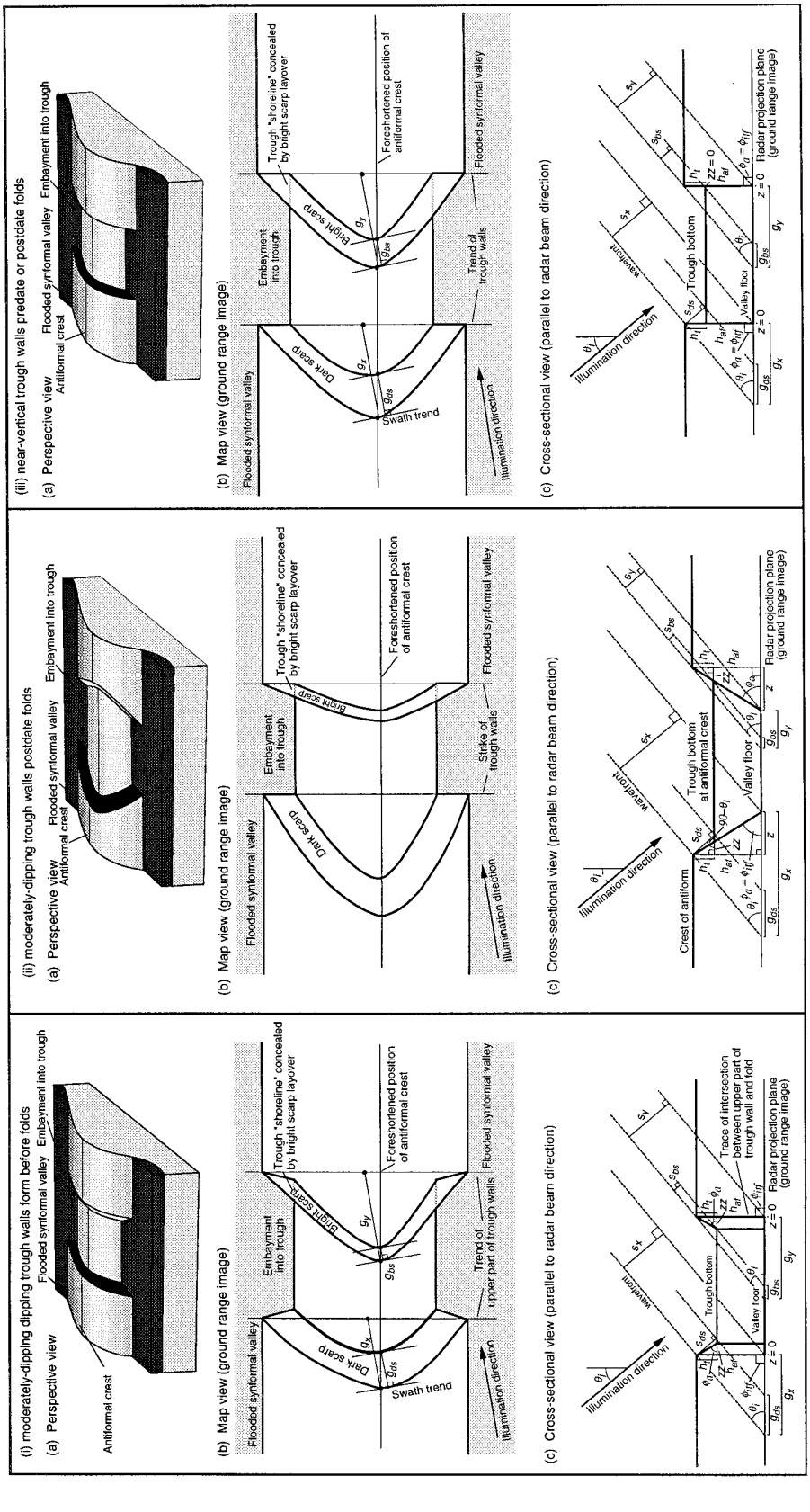

FIG. 6. Diagrammatic radargrammetric relations with deflection of fold-crossing troughs simulating moderately dipping trough walls form before folds (i), or after folds (ii), and vertically dipping trough walls formed before or after folds (iii). (a) Block diagrams, (b) ground range images, and (c) cross-sectional views parallel to radar beam direction (some aspects, such as the fold crest, are projected into the diagrammatic section). θ_i, incidence angle; s_x and s_y, slant range widths of deflections across the fold crest of the upper intersection between trough walls and the fold for radar-dark and radar-bright lineaments, respectively, as measured parallel to the radar beam direction; g_x and g_y, ground range widths of deflections across the fold crest of the upper intersection between trough walls and the fold for radar-dark and radar-bright lineaments, respectively, measured parallel to illumination direction; z, actual horizontal width (without distortion) of lineament deflections as measured parallel to the beam direction; h_{af}, height of antiformal crest above lava flow flood level; ϕ_{itf}, dip angle of the plane formed by the upper intersection between trough walls and the fold; s_{ds} and s_{bs}, slant range distances of radar-dark and radar-bright lineaments, respectively, measured parallel to the illumination direction; g_{ds} and g_{bs}, ground range widths corresponding to s_{ds} and s_{bs}, respectively; zz, actual horizontal widths of slopes measured parallel to beam direction; h_t, vertical height of trough walls (i.e., vertical depth of trough); ϕ_{as}, apparent slope angle measured parallel to beam direction.

wall intersection with the fold is shadowed (that is, the eastern, lower edge of the radar-dark lineaments is the edge of the shadow formed by the trough wall, not the actual intersection lineation between the lower part of the trough wall and the fold). From Fig. 6,

$$\phi_{itf} = \text{atn}\,(h_{af}/z), \tag{16a}$$

into which $z = (g_x - g_y)/2$ from Eq. (14) can be substituted, which yields

$$\phi_{itf} = \text{atn}\,[2\,h_{af}/(g_x - g_y)], \tag{16b}$$

where ϕ_{itf} is the dip angle of the plane formed by the upper intersection of the trough wall with the fold structure.

For the western trough locality at A, $h_{af} = 1.08$, $g_x = 2.1$, and $g_y = 1.88$ km, which from Eq. (16b) yields a dip of the plane described by the fold/upper trough wall intersection lineation of 84°. Values for the eastern trough are $h_{af} = 1.22$, $g_x = 2.33$, $g_y = 2.18$ km, thus $\phi_{itf} = 86°$. For locality B, $h_{af} = 1.94$, $g_x = 3.74$, and $g_y = 3.36$ km, yielding $\phi_{itf} = 84°$. Again, these estimates are minimum slope angles due to mass wasting processes. Thus, the steep angle of ϕ_{itf} eliminates one model outright—the trough walls cannot be graben-bounding normal faults formed after folding. With that model, we would expect shallower angles, ~60°. Recall that this option was already dismissed on the basis of parallelism of opposite trough walls as they cross the fold crests (Fig. 3). Radargrammetric calculations of ϕ_{itf} cannot differentiate between other models, but in concert with slope angle determinations using slope widths, which indicate steep slope angles, this analysis favors near-vertical trough walls. Timing of trough formation relative to folding is addressed later.

Additional three-dimensional information can be gained from embayment relations at flooded synform and ribbon trough valleys (Fig. 6). We assume that low-viscosity flood lava defines a horizontal plane in the synform valley and ribbon trough valleys, consistent with the radar-dark and thus smooth character of the valley fill. Although slight tilting could have occurred as a result of tectonism, assumption of horizontality over a few tens of kilometers is reasonable. Assuming that the lava surface remains essentially horizontal, the "shoreline" of the valley fill would also be horizontal. The horizontal valley fill intersects tilted structural elements and forms the shoreline trace. Because radar foreshortening or elongation does not result in relative shifts between points of equal elevation, the shoreline remains unmodified by radar imaging, except where the bright lineaments representing eastern trough walls overlay and thus conceal the eastern parts of the embayed trough shoreline (Fig. 6b). Radar-dark lineaments that define western trough walls are shifted to the west, leaving the western shoreline of the trough valley unchanged. The

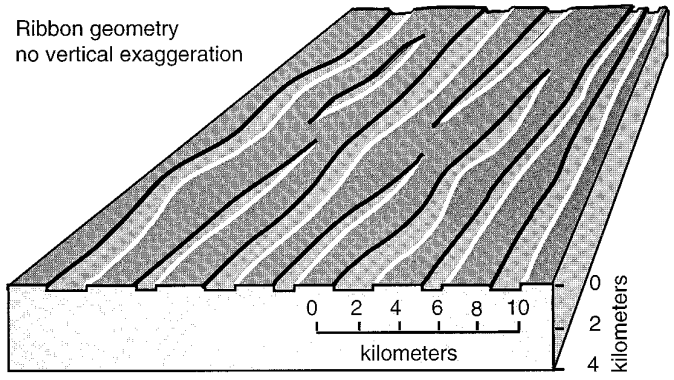

FIG. 7. Block diagram illustrating surface constraints on ribbon geometry. No vertical exaggeration.

east-trending part of the unmodified shoreline records the strikes of the fold limbs, ribbon ridge tops, and trough floors. The north-trending part of the unmodified shoreline records the strike of the western trough walls. The parallelism between the trend of the fold crests and the fold-limb strikes indicates that the folds are nonplunging and cylindrical along most of their length. Due to dip projection relations (Mankin 1950), the trace of the shoreline effectively preserves a sectional view of the ribbons (a two-dimensional slice through the three-dimensional ribbon-fold structure) (Fig. 6). The east-trending parts of the unmodified shoreline that define the ridge crests parallel the east-trending parts of the unmodified shoreline that mark the trough bottoms, indicating that the ridges and troughs are flat-topped and flat-bottomed, respectively, and that the troughs lack interior structures within image resolution.

RIBBON FORMATION AND TEMPORAL RELATIONS

The temporal relations of ribbon and fold formation are considered together with models of ribbon formation. Because structures mechanically modify a material, the way in which structures interact with one another depends on their relative timing relations as well as the mode of formation of each type of structure. Therefore, understanding the relative timing of structures typically requires understanding how the respective structures form and what the structures represent (that is, are the structures folds, faults, or fractures?). Any model of ribbon formation must account for each of the following constraints regarding ribbon geometry (Fig. 7). (a) Ribbon-forming lineaments exhibit sharp contrasts relative to adjacent materials. (b) Ribbon-bounding lineaments form a distinct pattern alternating between radar-dark and -bright, which represent trough walls oriented away from and toward the satellite, respectively. (c) Ribbons form long (30 to >170 km), narrow troughs (1.2-km mode) that alternate with parallel,

narrow ridges (1.2-km mode); ridges and troughs display extreme length : width aspect ratios. (d) Ribbon troughs are bounded by parallel, matched walls that would exhibit a close fit if the troughs were closed. In contrast, ridge walls are neither parallel nor matched. (e) Walls on opposite sides of a trough merge laterally terminating in a V. (f) Walls are near-vertical. (g) Troughs are ~0.25 km deep with consistent shallow depth along individual troughs and in adjacent troughs. (h) Trough floors are smooth and flat, lacking small-scale interior lineaments. (i) The trace of the shoreline of troughs and ridges parallels the fold crests.

The near-vertical orientation of the trough walls allows us to rule out a number of models for ribbon formation before or after folding, including ribbon formation by folding, strike-slip faulting, thrust faulting, and classic 60° fault-bounded graben formation, as discussed below.

Fold Model

A fold model may satisfy, under extremely special conditions, some of the ribbon constraints, but overall a fold model fails. The ribbon cross section and planform would require long, linear, isoclinal box folds, with sharp kinks (nearly 90°) and flat-floored synform troughs and antiform crests, with equal amplitude along individual folds and among adjacent folds. Furthermore, the folds would have to be cylindrical and nonplunging along their entire length. We are not aware of a way for a fold model to accommodate the matching of trough walls (constraint (d)) or V-shaped terminations (constraint (e)). In addition, folds on Venus typically exhibit smaller aspect ratios, they have gradational rather than sharp tonal changes, implying curved geometry, and they typically host smaller-scale folds (e.g., Solomon *et al.* 1992, Suppe and Conners 1992). In that the ribbon structures exhibit no characteristics typical of folds, we dismiss a fold origin for ribbons.

Classic Fault Models

Classic fault theory predicts dips of ~60° for normal faults, ~30° for thrust faults, and vertical for strike-slip faults (Anderson 1951). The near-vertical dips of the trough-bounding structures are difficult to accommodate within classic thrust-fault or normal-fault models; we dismiss ribbon formation by classic thrust or normal faults. Strike-slip faults are commonly steep, but displacement along strike-slip faults would not result in alternating ridges and troughs, thus ribbon formation by strike-slip faulting can be ruled out. Furthermore, strike-slip faults forming after folds would result in offset of fold crests and troughs, which is not observed. Thus, we rule out ribbon formation by displacement along numerous strike-slip faults.

Shear and Tensile Fractures

Steep faults may result under near-surface transitional-tensile failure conditions or due to reactivation of steeply oriented pre-existing weaknesses (e.g., McGill and Stromquist 1979, Price and Cosgrove 1990); near-vertical trough walls could also result from the opening of tensile fractures (e.g., Pollard and Aydin 1988) of a brittle membrane above a ductile substrate (Hansen and Willis 1996). Thus, with respect to ribbon structure–fold formation we consider four possibilities: that ribbons result from displacement of a brittle layer along shear fractures resulting in steep-sided graben (shear-fracture ribbons) that formed either (1) before or (2) after the folds, and that ribbons result from the opening of tensile fractures (tensile-fracture ribbons) within a brittle membrane above a ductile substrate, with fracturing and opening predating (3) or postdating (4) fold formation.

Ribbon structures preserve a periodic spacing or wavelength (Fig. 1d; Table I) that can be treated as a wavelength layer instability. Ramberg (1955) noted an apparent relationship between dominant wavelength and the thickness of layers of boudinage structures (Lohest 1909), structures formed by brittle or ductile layer-parallel extension. This dominant wavelength/thickness relation has been explored empirically, experimentally, and theoretically by a host of workers (see discussion by Price and Cosgrove (1990) and references therein). Ribbon ridges and troughs are regularly spaced with extreme aspect ratios, and thus they are similar to boudins and intervening boudin lines, respectively. Boudins are cylindrical periodic layer instabilities that result from the failure of a competent layer sandwiched between weaker layers; layer-normal compression results in layer failure and subsequent boudin separation along periodically spaced boudin lines (Ramberg 1955). In the case of ribbon structures, the upper weak layer would be the Venus atmosphere and the lower weak layer is a ductile substrate or crust.

Within the field of structural geology, a range of structures with variable brittle to ductile character have been referred to as boudins (e.g., Price and Cosgrove 1990). Herein we are concerned with boudins in which the competent layer fails in a brittle fashion (the sharp geometry of ribbon ridges and troughs is consistent with brittle failure and inconsistent with ductile failure) along either tensile fractures, resulting in rectangular (in cross section) or extension fracture boudins, or shear fractures, resulting in rhombohedral (in cross section) or trapezoidal boudins (see review by Lloyd *et al.* 1982). The type of failure, whether along tensile fractures or shear fractures, is a function of the tensile strength of the material and the magnitude of the differential stress (Lloyd *et al.* 1982). Boudin width is governed by the tensile strength and thickness of the competent layer and the strain rate in the matrix (Ramberg 1955, Price and Cosgrove 1990). Field experimental studies show that dominant boudin width/layer thickness ratios ranges from 2 to 4 (Stromgard 1973, Ekström 1975, Kidan and Cosgrove 1996). Although Tal-

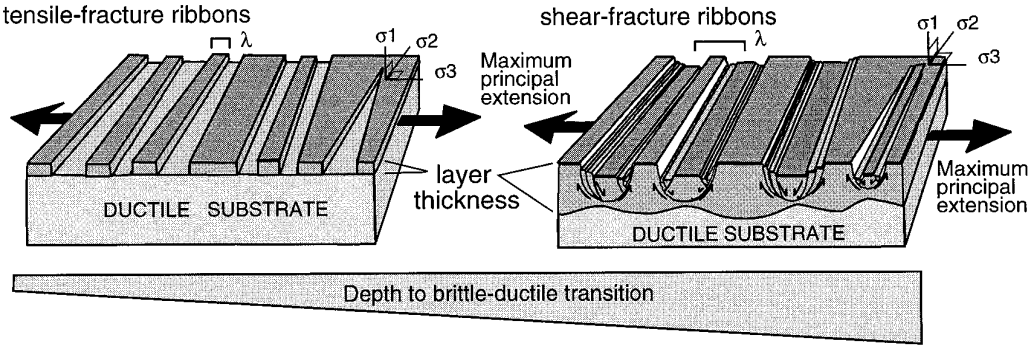

FIG. 8. Block diagrams illustrating end-member tensile-fracture ribbon and shear-fracture ribbon models and dominant wavelength, λ. σ_1, σ_2, and σ_3 are maximum, intermediate, and minimum principal compressive stresses, respectively. Ribbon trough formation, whether by opening of tensile fractures or by trough formation by normal faults, requires a ductile substrate at relatively shallow depth. Opening of tensile fractures would be favored with a sharp brittle–ductile transition (BDT) at shallower depth, whereas a broader and deeper BDT would favor shear-fracture ribbon structures.

bot (1970) reported width/thickness ratios ranging from 2 to 20 for quartz veins deformed under ductile conditions, and Smith (1975, 1977, 1979) outlined a mathematical analysis of layer wavelength instabilities which predicts boudin width/thickness ratios from 4 to 6, these analyses treat pinch-and-swell structures, which involve ductile flow and necking but no fracturing.

We use boudin width/layer thickness ratios of 2–4 to estimate the layer thickness for ribbon structures, whether formed by shear fracturing (shear-fracture ribbons) or tensile fracturing (tensile-fracture ribbons) because the observed steep trough walls are indicative of brittle rather than ductile deformation at the surface. Competent layer thickness in turn represents an estimate of the depth to a weak layer below the strong fractured layer, or the depth to a crustal brittle–ductile transition (BDT). Using width/layer thickness ratios of Talbot (1970) and Smith (1977) would result in shallower estimated depths to BDT.

In the case of tensile-fracture ribbons, the dominant wavelength is equal to fracture spacing or ridge width (Fig. 8). Using the dominant ridge width at southwestern Fortuna (1.2 km) results in a layer thickness and thus depth to BDT of ~0.3–0.6 km. Lloyd *et al.* (1982) proposed that the important wavelength for tensile-fracture boudins is the *minimum* wavelength rather than the dominant wavelength based on stress transfer theory which predicts that boudins develop by successive ''mid-point'' fracturing until a layer is reduced to segments (boudins), which are all shorter than the critical length, a function of tensile strength of the layer. Using minimum wavelength (minimum ridge width) of 0.8 km (Table I) results in an estimated layer thickness and hence depth to BDT of ~0.2–0.4 km. These estimates to BDT are similar to estimates of trough depth determined through radargrammetric analyses (~0.25 km mean).

In the case of shear-fracture ribbons, we take the dominant wavelength as a measure from graben center to graben center (Fig. 8). This is a maximum estimate of wavelength (and therefore it yields a maximum layer thickness) because it is a function of both initiation wavelength and the amount of finite extension across the graben valleys. Therefore, estimates to BDT using this wavelength will yield maximum BDT depths, and the actual depth to BDT at the time of ribbon formation would have been shallower. If we treat southwest Fortuna ribbons as shear-fracture ribbons, the dominant wavelength is simply dominant ridge width plus dominant trough width (ridge width plus midway across the trough on either side) measured from SAR images (Table I). Within the study area, the dominant ridge width is 1.2 km and the dominant trough width is 1.2 km, resulting in a maximum dominant wavelength of 2.4 km and an estimated depth to BDT of 0.6–1.2 km if these ribbons formed due to failure along shear fractures. Geometric relations preserved at southwest Fortuna Tessera are better interpreted as resulting from tensile-fracture ribbons, and thus estimates of layer thickness assuming a shear-fracture mechanism for southwest Fortuna ribbons provide a maximum depth to BDT.

The critical factor that results from this analysis is that the presence of ribbon structures, whether initiated as shear fractures or tensile fractures, require that the depth to crustal BDT during ribbon formation must have been quite shallow (<1.2 km, and likely ~0.2–0.4 km) based on the ribbon wavelengths measured at southwest Fortuna. Therefore, ribbon structures require the presence of a weak layer at relatively shallow depth across the entire region over which ribbon fabrics develop.

Broad-wavelength folds are spatially correlated with ribbon structures at southwest Fortuna Tessera and across most highland plateaus (Hansen and Willis 1996). Folds can also be treated as layer wavelength instabilities with

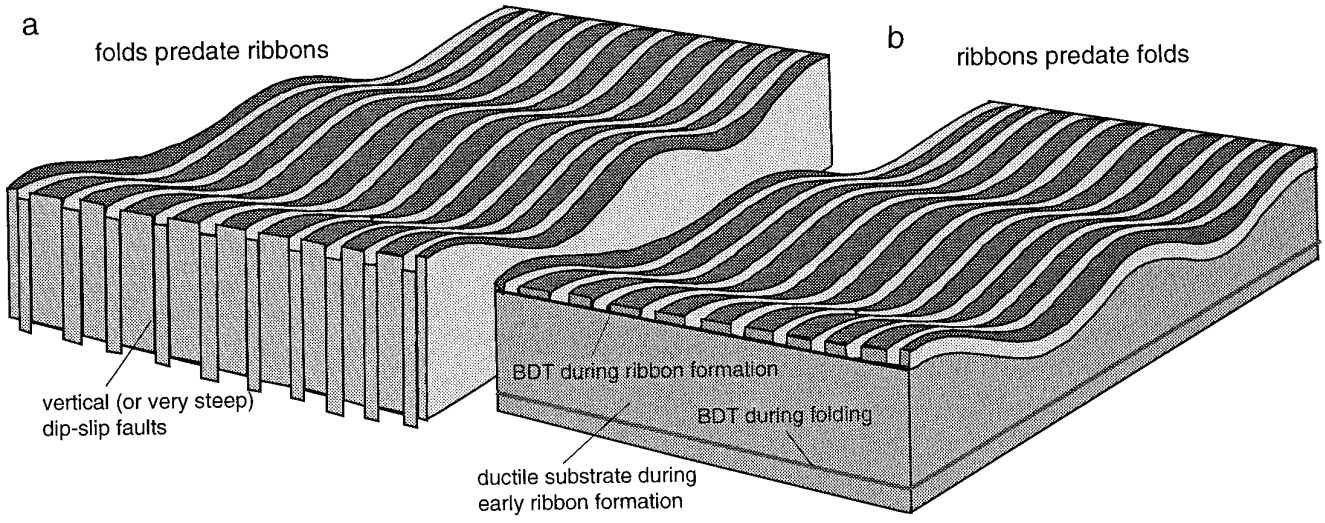

FIG. 9. Block diagrams illustrating temporal relations between ribbons and folds. (a) If folds predate ribbons the crust must be dissected by closely spaced (1.2-km mode), near-vertical faults. (b) Ribbons predate folds and form as the result of opening of tensile-fractures ribbons, or displacement along shear fractures within a brittle membrane above a ductile substrate (see Fig. 8). The depth to the brittle-ductile transition (BDT) increases with time and fold formation. The plastic–viscous transition is at ~6 km depth at the time of fold formation (Brown and Grimm 1997).

characteristic ratios of dominant wavelength to layer thickness. The long wavelength of the folds (15–30 km) relative to the ribbon structures suggests that the folds require a deeper depth of support (Hansen *et al.* 1996). Using a dominant fold wavelength of 15 km and layer instability theory, Brown and Grimm (1997) estimated a depth of ~6 km for the crustal plastic–viscous transition during the formation of broad highland plateau folds, providing strong support for the above statement. Because the folds require a significantly deeper depth of support than the ribbons, the simplest history involves one in which the folds formed after the ribbons. That is, that structures requiring the shallowest BDT form first and structures reflecting a deeper BDT form later. If structures requiring a deeper BDT form first, one must justify how early formed structures could be supported as the BDT shallowed for the formation of the structures that reflect a shallower BDT.

If the ribbons, which require a very shallow depth to BDT (<1.2 km, and likely ~0.2–0.4 km for southwest Fortuna), formed after the folds, which require support at a depth of ~6 km, the folds would not be supported. Thus, whether ribbon structures initiated as shear fractures or tensile fractures of a brittle layer, ribbons predate fold formation, and we can rule out options 2 and 4, that ribbons formed by shear-fracture graben (with steep or moderate dipping structures) or by opening of tensile fractures *after* the folds (Fig. 9). Recall that option 2 was already ruled out on the basis of ribbon-fold geometry (Fig. 3). Formation of the ribbons as down-dropped graben with slip along near-vertical faults would require dissection of the crust along closely spaced (~1.2 km, ridge width mode) near-vertical faults cutting through a strong crustal layer greater than ~6 km thick (the thickness of the layer required to support the observed fold wavelengths) (Fig. 9a). However, the thickness of the strong layer (~6 km) is in sharp contrast with the layer thickness predicted by wavelength/layer thickness instability arguments for the ribbons discussed above. In addition, dip–slip displacement along these closely spaced faults would not accommodate the V-terminations of trough walls observed at southwest Fortuna Tessera. Furthermore, dissection of the crust illustrated in Fig. 9a would result in very little, if any, extension of the crust, and the forces responsible for such deformation over thousands of square kilometers are difficult for the authors to envision.

One might argue that ribbons could initiate as shear or tensile fractures after folding *if* a shallow layer that could accommodate flow was present at depth between a shallow brittle layer and a deep strong layer. Indeed, McGill and Stromquist (1979) documented an evaporite layer at a depth of ~0.5 km under ~160 km^2 in the Canyonlands (western USA), where steep-sided graben reactivate pre-existing joints. However, it is difficult to imagine what might form such a layer on Venus. Furthermore, the widespread nature of ribbon terrain across highland plateaus (e.g., Hansen *et al.* 1997, Ghent and Hansen 1997), which individually cover hundreds of thousands of square kilometers, would require that such a weak layer be present in several areas, each of which are many orders of magnitude greater than that of the Canyonlands. Furthermore, if the rheological structure of the crust during ribbon formation consisted of a weak layer sandwiched between a thin strong

layer above and a strong layer below, as exists at the Canyonlands, two distinct deformation wavelengths with trends parallel to the ribbon structures would be expected to form (e.g., Zuber 1987), yet such structures are not observed. Therefore, without independent data that might suggest the presence of such a weak layer we dismiss this option from further consideration. Therefore, ribbon structures likely formed prior to fold formation, whether they formed by tensile or shear fracturing and subsequent extension of a thin brittle layer above a ductile substrate.

An example of tensile-fracture ribbons. At southwestern Fortuna Tessera the close fit of opposite walls of individual troughs (constraint (d)) and their V-shaped terminations (constraint (e)) indicate that these ribbon structures initiated as tensile fractures. If ribbons resulted from the opening of tensile fractures within a brittle layer above a sharp BDT over a ductile substrate, such as a brittle chocolate layer above a caramel base, all the observed geometric and structural constraints could be met. In the case of tensile-fracture ribbons, trough walls would have been originally connected along near-vertical tensile fractures and separated due to extension and trough formation, thus the trough-bounding bright and dark lineaments would be matched, near-vertical structures that merge into V-terminations, as observed. The structures on either side of a ridge would represent two separate fractures; therefore, they would not be expected to be matched or parallel. The lineaments that represent the trough walls would show sharp contrast changes with adjacent material. The troughs would be flat-bottomed and smooth providing a minimum estimate of brittle layer thickness. The brittle boudin ridges might lie completely above a ductile substrate or they might subside into the substrate depending on the strength of the substrate (a function of material viscosity, strain rate, and temperature) at the time of ribbon formation and the mass of the ridge boudin—topics beyond the scope of the present study. Ridge width defines structural wavelength and is a function of tensile strength and layer thickness.

Locally within southwestern Fortuna Tessera some ribbons show double-bright or double-dark lineaments with one of the double-bright or double-dark lineaments shorter than the other (Fig. 2). We interpret these lineaments to represent secondary tensile fractures that formed with continued extension and a progressive increase in the depth to BDT with time (Fig. 10); that is, a downward migration of the elastic–ductile front with time. Thus, the double-bright or double-dark lineaments are interpreted to represent tensile fractures that formed within preexisting tensile-fracture ribbon troughs.

An example of shear-fracture ribbons. At Thetis Regio ribbon structures show extreme aspect ratios (up to 40 : 1), although alternating ridge and trough morphology is not as well defined as at Fortuna. In addition, the trough walls

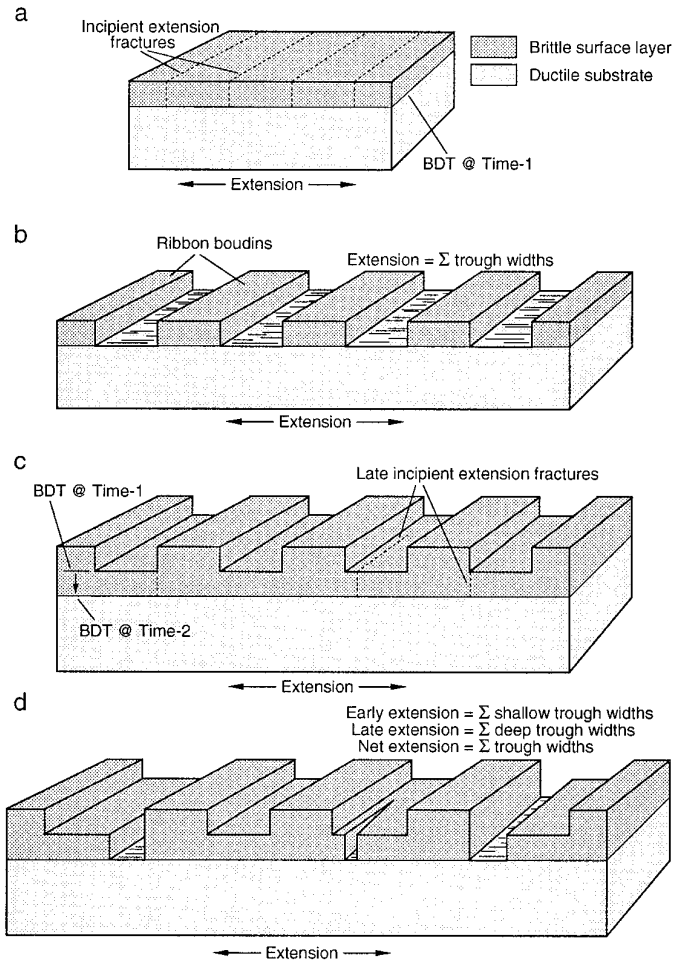

FIG. 10. Block model illustrating formation of double-dark or double-bright radar lineaments at southwestern Fortuna Tessera.

at Thetis Regio are defined by a series of subparallel lineaments, and trough floors ramp up to join trough walls displaying parallel rather than V-shaped terminations (Fig. 11). These features would be expected if ribbon troughs represent high-angle normal fault-bounded graben that initiated along transitional tensile-shear fractures or shear fractures (Fig. 8). Space problems inherent to graben formation require accommodation faults, rollover folds, and/or differential tilt between horst and graben blocks (e.g., Price and Cosgrove 1990, Twiss and Moores 1992); the trend of graben walls are parallel, but not matched, and graben floors ramp up to join border faults along strike (e.g., McGill and Stromquist 1979, Suppe and Connors 1992). We interpret that the Thetis ribbon structures initiated as shear fractures and are dominantly steep-sided graben with interior lineaments representing accommodation structures (Fig. 8). Steep graben of the Canyonlands show similar accommodation structures, tilted blocks, and trough walls which cannot be closed—all features that

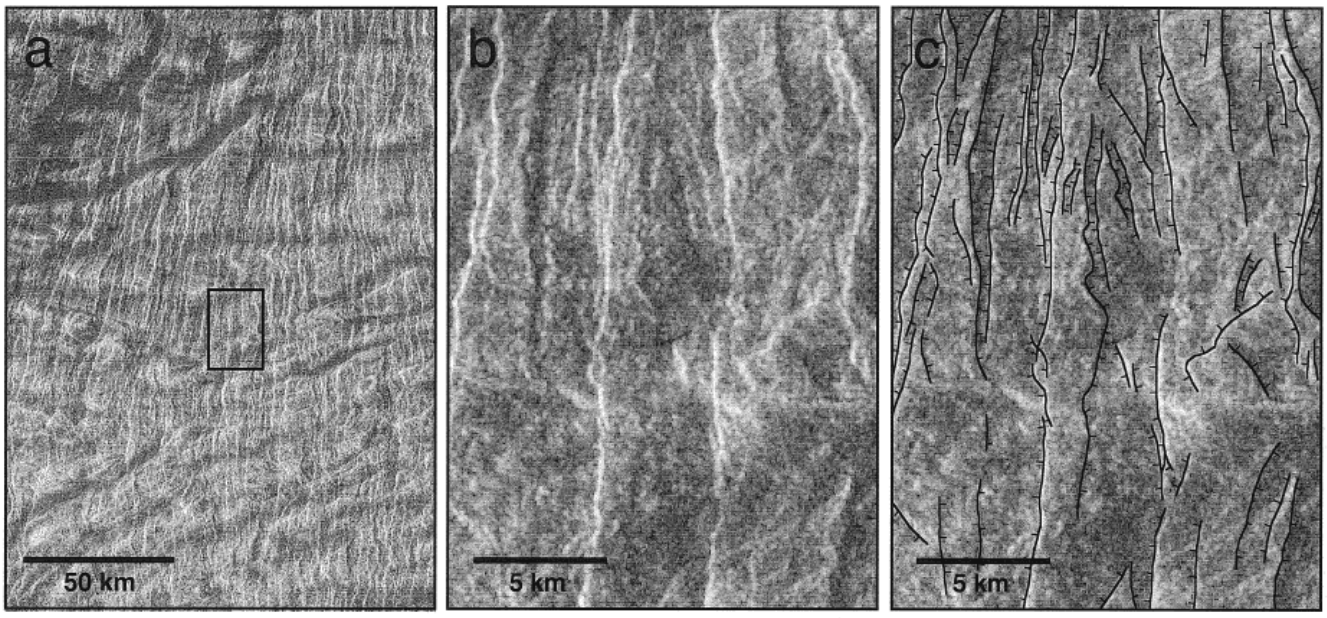

FIG. 11. SAR image (a) of ribbons at northeast Thetis Regio (centered at 06.7°S, 131.05°E); (b) detail of the area of box in constraint (a); (c) map of ribbon structures in constraint (b); hatched lines delineate trough walls with ticks on the trough side. Trough floors ramp up to join ridge tops as the troughs end. Opposite trough walls do not show the distinct pairing present at southwestern Fortuna Tessera, although the distinctive extreme aspect ratios of ribbon structures are apparent (a).

reflect graben asymmetry and shallowing of the faults at depth (Trudgill and Cartwright 1994, Moore and Schultz 1996, Moore *et al.* 1997). The dominant wavelength (ridge plus trough) is more difficult to estimate at Thetis because ridges and troughs do not alternate with the regularity that the Fortuna ribbons show. Our estimates of dominant wavelength range from 3.5 to 4.5 km, resulting in a depth to BDT of ~0.9–2.25 km. Again, this is a *maximum* estimate to BDT because the dominant wavelength (graben center to graben center) includes finite extension, and therefore the initial wavelength of graben center to graben center prior to layer extension must have been less. For example, if Thetis ribbons record 10% extension, the initial dominant wavelength (dominant wavelength prior to extension) would be 3.5–4.5 km less 10%, or ~3.1–4 km, resulting in an estimated layer thickness (and depth to BDT) of 0.78–2 km. If greater than 10% extension is recorded by the Thetis ribbons, then the estimated depth to BDT during ribbon formation would be even shallower. Although the depth to BDT is somewhat deeper than the BDT at southwest Fortuna, it is still quite shallow, and significantly shallower than the ~6 km depth of support required by highland plateau folds (Brown and Grimm 1997). Due to space problem considerations, shear-fracture ribbons, such as those at Thetis Regio, might shallow into a broader BDT, rather than the sharp BDT expected for ribbons structures that initiated as tensile fractures. Incipient ductile flow might be expected at depth; the presence of which might argue for the use of the dominant wavelength/thickness ratios of 4–6 (Smith 1977), which would result in a shallower estimated depth to BDT (0.6–1.13 km) during Thetis Regio ribbon formation.

Tensile-fracture ribbons and shear-fracture ribbons represent end members, both of which are present on Venus (Fig. 8). In either case, ribbon-trough formation requires extensional strain of a strong thin layer above a ductile substrate. Furthermore, ribbon structures require a shallow BDT and thus they most likely predate the formation of long-wavelength folds with which they are commonly spatially correlated. The important wavelength for tensile-fracture ribbons is the minimum ridge width; the maximum critical wavelength for shear-fracture ribbons is the dominant ridge width plus the dominant trough width. The character of ribbon structures may provide clues to the dominant style of deformation responsible for their formation. Tensile-fracture ribbons should show distinct alternating bright and dark lineaments (with sharp contrast with adjacent materials) (constraints (a) and (b)), matched and parallel trough walls that display a close fit (constraint (d)), V-terminations (constraint (e)), and a lack internal lineaments (constraint (h)). Shear-fracture ribbons display interior lineaments, lack distinct alternating ridge and trough morphology, and trough walls that cannot be closed. In addition, shear-fracture ribbon troughs should show parallel terminations with the trough floor ramping up to meet the ridge tops. In both cases, ribbon fabric is

distinguished on the basis of long (10–100 km), narrow (~1–3 km), closely spaced, alternating ridges and troughs. The extreme aspect ratio of these structures and the cylindrical periodic ridge–trough morphology distinguishes ribbon fabrics from other deformation features on Venus. In the case of tensile-fracture ribbons, trough width is a direct reflection of finite surface layer extension, and the direction of maximum finite extension is normal to the regional ribbon trend, unless there are two populations of ribbons defined by different orientations. In this case one set of ribbons may predate the other, or the two ribbon sets may have formed essentially synchronously as chocolate-block boudins (e.g., Ghosh 1988). In the case of shear-fracture ribbons, finite extension is a function of the shape of the faults, trough width and depth, ridge spacing, and layer thickness; if the shear fractures that form the trough walls represent reactivated structures, maximum elongation may be at a slight angle to a direction perpendicular to the regional ribbon trend. Estimates of extension recorded by shear-fracture ribbons are developed elsewhere (Ghent and Hansen, in preparation).

IMPLICATIONS OF TENSILE FRACTURES

Geometric relations at southwestern Fortuna Tessera indicate that these ribbons result from tensile fracturing of a thin, brittle membrane above a ductile substrate. In order for failure to occur primarily by opening of vertical tensile fractures maximum compressive stress must be vertical, and the crust must be virtually intact with few, if any, pre-existing fractures (Sibson 1985, Golombek and Banerdt 1986, 1990). But how could it be possible that thousands of square kilometers much less hundreds of thousands of square kilometers of Venus could be virtually intact and free of fractures? Surely there is evidence for structural discontinuities at scales <10 km essentially everywhere on Venus as evidenced by Magellan SAR imagery (Solomon *et al.* 1992). Nowhere on Venus can one locate a large region that is fracture free. Furthermore, if one could locate such a region, one must reasonably assume that the surface is composed of basalt, which itself is likely to host columnar cooling joints, even if they are below SAR resolution. Because jointing may nucleate in basaltic lava cooled to 725°C (Ryan and Sammis 1981), Venus lava flows should have a fully developed network of cooling joints once the flow interior has cooled below ~600°C (Schultz 1993). So it seems highly unlikely that tensile fractures could form over areas of hundreds of thousands of square kilometers on Venus, and yet they seem to have done just that.

What if a region of Venus was somehow mechanically annealed of all, or essentially all, preexisting fractures prior to ribbon terrain formation? The tensile ribbons at southwestern Fortuna Tessera require a very shallow depth to BDT (0.17–0.4 km), and the presence of spatially correlated long-wavelength folds indicates that the depth to BDT increased with time. Rheology, and hence the BDT, is most strongly affected by composition, temperature, fluids, and strain rate. The simplest way to increase the depth to BDT with time over a large area is through thermal decay. Presumably, if a BDT could be as shallow as 0.17–0.4 km, it could also have been at or near the surface. If a BDT is at or near the surface preexisting fractures would become annealed.

In order to become annealed, basalt would have to experience conditions which would allow ductile behavior, or creep. Ryan and Sammis (1981) estimated that for Hawaiian olivine tholeiite at 1 atm pressure the principal mechanical responses are (1) elastic ($T \leq 600$°C), (2) reduced creep ($600 < T < 725$°C), (3) glass transition ($T \sim 725$°C), (4) enhanced creep ($725 < T < 980$°C), and (5) partial melt ($T > 980$°C). We can use these values for Venus with some qualification. Surface pressure on Venus is 92 MPa, which should lead to a slight increase in the strength of the rock and therefore to an increase in the critical temperatures above (Schultz 1993). In addition, the presumed dryness of venusian basalt (Kaula 1990) should also result in an increase in critical temperatures above Hawaiian tholeiite. Strain rate is presumably unknown, although strain rate might change as a result of a tectonic process and therefore provide a means (or the cause) by which a cooling basalt surface, with a downward migrating rheological/mechanical front, could change from, say, ductile creep to brittle fracturing. Although, such a change in strain rate would not be required. Annealing requires ductile (creep) behavior; tensile fracturing and ribbon formation require brittle (elastic) behavior. Thus, at temperatures of $\sim 600 < T < 980$°C (or higher due to factors mentioned above), venusian basaltic crust might be mechanically annealed and brittley fractured with subsequent cooling.

Well-established Griffith failure criteria explains the formation of tensile fractures and shear fractures in intact rock (e.g., Jaeger and Cook 1979, Price and Cosgrove 1990). Griffith failure criterion assumes that fracturing initiates at the tips of small, open cracks that are inherent in rocks. Tension cracks form at low confining pressure, where minimum principal stress (σ_3) is equal to the tensile strength, T_0, of the rock (tensile stress is negative, compressive stress is positive in our discussion). Values of T_0 for intact basalt at ambient temperature range from -10 MPa to -30 MPa, with an average of -14 MPa (Tanaka and Golombek 1989, Schultz 1993). At elevated temperature (700°C), T_0 for basalt is -30 MPa (M. P. Ryan, unpublished data cited by Schultz 1993) consistent with a rapid increase in tensile strength and fracture toughness as documented for silicate ceramics at high homologous temperatures (see review by Schultz 1993). The tensile strength of basalt

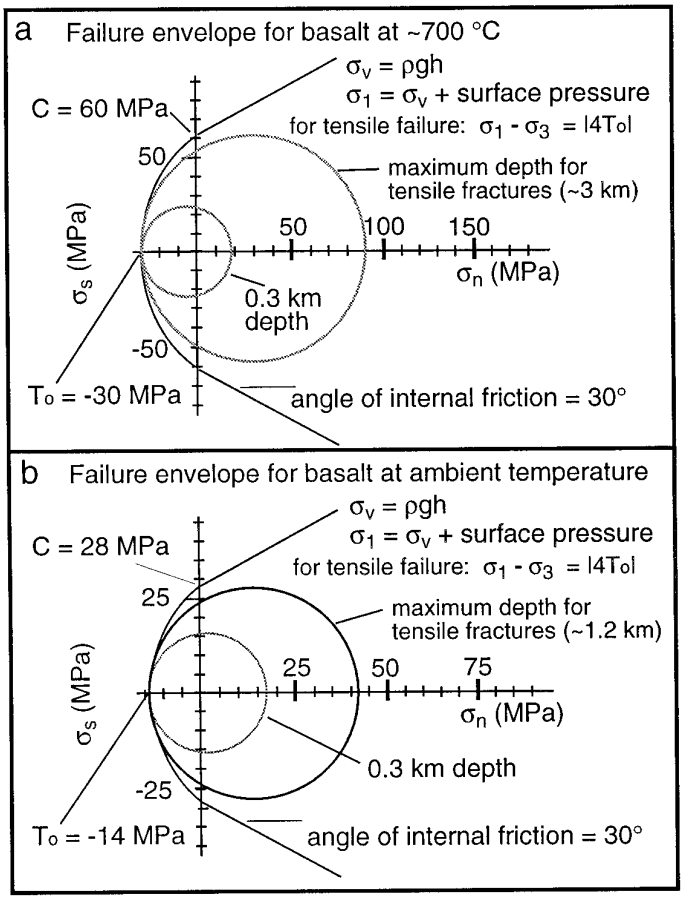

FIG. 12. Mohr–Griffith failure envelope for basalt at (a) ~725°C using $T_0 = -30$ MPa (Schultz 1993), angle of internal friction is 30° (Hubbert and Rubey 1959), and cohesion, $C = 2\ T_0$ (Brace, 1960); and (b) $T_0 = -14$ MPa (ambient temperature; Schultz 1993), angle of internal friction is 30°, and $C = 2\ T_0$. Use ribbon depth is 0.3 km and basalt density is 3.0 g/cm^3 to estimate vertical stress (σ_v). Given these conditions the rock should fail along tensile fractures, unless preexisting fractures are favorably oriented with respect to a frictional sliding envelope.

probably remains constant up to a critical temperature associated with increase crack-growth resistance and partial melting, ~725°C (Ryan and Sammis 1981). Following Brace (1960), the Griffith failure envelope within the tensile field can be estimated as the parabolic form with cohesion, C, twice tensile strength. Using values of −30 and 60 MPa for tensile strength and cohesion (in moderate agreement with Brown and Grimm (1996) who estimate cohesion to be 50 MPa for Venus basalt), respectively, and an angle of internal friction of ~30° (a reasonable estimate for basalt, Hubbert and Rubey 1959), we can construct a failure envelope for intact basalt at ~725°C (Fig. 12a). Using a ribbon depth of 0.3 km (determined from radargrammetric analysis) and basalt density of 3.0 g/cm^3 we can estimate vertical compression (~8 MPa). Adding to this the surface pressure on Venus (9.2 MPa) we arrive at a value for maximum compressive stress, σ_1, at ribbon structure depth. Using this value of σ_1, failure requires that minimum compressive stress, σ_3, is tensile, and the failure must be along vertical tension fractures (Fig. 12a). Values of −14 and 28 MPa for tensile strength and cohesion, respectively, similarly result in failure along tensile, rather than shear fractures (Fig. 12b); shear fractures would form at depths greater than ~1.2 km. Therefore, the Mohr–Griffith analysis illustrates that failure along tensile fractures is predicted for ribbon depths at southwest Fortuna Tessera. The tensile fractures would open into extension fractures with continued extension. Assuming a homogeneous, isotropic, brittle surface layer (as required by tensile fractures), maximum elongation is perpendicular to the trace of the ribbons and is recorded by trough widths. Profiles across portions of southwestern Fortuna Tessera reveal elongation of ~60–85% (Table I; see also Pritchard *et al.* 1997).

If the Mohr stress circle intersects the failure envelope anywhere along the curve with a nonzero shear stress, that is if $\sigma_1 - \sigma_3 > |4\ T_0|$, shear fractures will form; if $\sigma_1 - \sigma_3 < |4\ T_0|$, tensile fractures will form (Price and Cosgrove 1990). Therefore, we can also calculate a maximum depth for tensile fracture formation (~3 km if $T_0 = -30$ MPa ($T \sim 700$°C); ~1.2 km if $T_0 = -14$ MPa). These calculations imply that tensile-fracture ribbons will form if the elastic layer is thinner than these values, and shear-fracture ribbons will form if the elastic layer is thicker than these values. Thus, Griffith failure analysis indicates that tensile fractures are both mechanically feasible and most likely to form at the shallow depths documented for ribbon structures. Shear-fracture ribbons might form due to brittle deformation of a relatively thicker layer (greater σ_1), or they might form at lower temperature and therefore lower tensile strength.

In summary, ribbon fabrics represent tensile or shear fracturing of a thin membrane above a ductile substrate. The region of ribbon fabric must have been mechanically annealed prior to ribbon formation, requiring temperatures of >~725°C. Mechanical annealing (BDT at the surface) would have wiped out all preexisting fractures, including any earlier tectonic deformation and fractures due to impact cratering. As regions prepared in this manner cooled, the thin elastic membrane at the surface apparently experienced tensile stresses, resulting in the formation of tensile or shear fractures (depending on elastic layer thickness and tensile strength, a function of temperature). Continued extension resulting in opening of these fractures, formed the alternating trough and ridge morphology that is characteristic of ribbon fabrics. The depth to the BDT continued to increase with depth with time, as recorded by the deeper depth required to support broad folds which are spatially correlated with ribbon fabrics.

IMPLICATIONS FOR HIGHLAND PLATEAU FORMATION AND LITHOSPHERE EVOLUTION

Ribbon structures occur within each of Venus' highland plateaus except central Phoebe Regio, and therefore the presence of this distinctive structural fabric places important constraints on highland plateau evolution. Highland plateaus are quasicircular with diameters ranging from ~1700 to 2500 km. They are steep-sided and flatted-topped regions characterized by tectonic deformation. Geophysically, highland plateaus are marked by small gravity anomalies, low gravity to topography ratios, and shallow apparent depths of compensation, <100 km and typically <50 km (e.g., Herrick *et al.* 1989, Smrekar and Phillips 1991, Bindschadler *et al.* 1992b, Simons *et al.* 1994, Grimm 1994, Herrick 1994), indicating isostatic compensation by thickened crust (35–45 km; Grimm 1994, Simons *et al.* 1997).

Two general end-member models have been proposed for the formation of plateaus: ''hotspot'' or mantle upwelling, and ''coldspot'' or mantle downwelling (for review see Bindschadler *et al.* 1992, Phillips and Hansen 1994, Bindschadler 1995, Hansen *et al.* 1997). In the case of downwelling, crustal thickening results from subsolidus flow or lithospheric accretion and should result in surface compressional stress and contractional strain during early stages of plateau evolution. In the upwelling case, crustal thickening results from magmatic underplating and should record surface tensile stress and extensional strain during early plateau evolution. Note that the upwelling model for highland plateau formation proposed post-Magellan (e.g., Hansen *et al.* 1996) differs from the upwelling model proposed prior to Magellan (e.g., Herrick and Phillips 1990, Phillips *et al.* 1991) in which it was proposed that volcanic rises evolve into highland plateaus, which is clearly not the case (Bindschadler 1995, Hansen *et al.* 1997).

The rheological evolution of the crust and the surface strain history as recorded by ribbon structures and spatially correlative folds are inconsistent with highland plateau formation by downwelling, yet might be predicted by highland plateau formation by magmatic underplating. Specifically, ribbon structures require (1) mechanical annealing of the crust prior to ribbon formation (BDT essentially at the surface), (2) widespread extension of a thin brittle membrane above a ductile substrate followed by limited contraction with a deeper depth to BDT, and (3) downward migration of the BDT with time during ribbon formation (BDT < 1.2 km) and subsequent fold formation (plastic–viscous transition at ~6 km).

Previous work by Bindschadler *et al.* (1992) proposes a strain history of early contraction followed by late minor extension within Ovda Regio, the largest of the crustal plateaus. Although these workers recognized ribbon structures (which they called steep troughs) as distinct from late graben which cut the crests of folds (which they called graben), these workers extrapolated the temporal constraints of the late graben relative to the folds to the ribbon structures because the ribbons (steep troughs) and graben generally parallel one another (both trending normal to the fold crests) in the region of northeastern Ovda Regio which they studied. These workers similarly extrapolated temporal relations between folds and ribbon fabrics (steep troughs) using late graben that cut the crests of Alpha, Tellus, and Thetis regiones. Hence, they interpreted the tessera fabrics to record early contraction followed by late extension. Similarity, or even parallelism, in structural trend does not constitute proof of synchroneity however, and the recognition of ribbon fabrics as a distinct suite of structures separate from the late graben requires a revised strain history as recorded by tessera fabrics comprised of spatially correlated ribbons, folds, and late graben (Ghent and Hansen 1997, Pritchard *et al.* 1997).

The impact crater record of highland plateaus is also consistent with highland plateau formation by magmatic underplating. Impact craters within highland plateaus are generally undeformed, or if they are deformed they are affected only by late graben (Gilmore *et al.* 1997). This relationship indicates that ribbon and fold formation predate all craters preserved within the highland plateaus. However, the absolute times of ribbon and fold formation are unconstrained. The strain imparted on the crust by ribbon and fold deformation is not particularly complex (Ghent and Hansen 1997). Therefore, evidence of craters that existed prior to ribbon and fold formation should be preserved—unless the craters were destroyed, not by ribbon and fold formation, but rather, by processes that lead to the formation of the ribbon structures. Ribbon fabrics require annealed crust, or at least a very shallow depth to BDT. Annealing would have wiped out preexisting fractures and preexisting craters. The shallow depth to BDT required for ribbon fabric formation would cause relaxation of earlier formed crater-related structures (Grimm and Solomon 1988). Therefore, highland plateau surfaces would not be able to record the effects of impact craters until late in highland plateau evolution when the crustal BDT had migrated to depths that could support impact craters. Thus, the lack of evidence for craters affected by ribbon structures is consistent with highland plateau formation by mantle upwelling and magmatic underplating.

In order for a heat source to be able to anneal mechanically the crust to the surface, the Venus lithosphere would have to be quite thin. Presently, the Venus lithosphere is ~100–150 km thick (Phillips *et al.* 1997), and volcanic rises, which represent the contemporary surface expression of mantle hotspots or upwellings (see review by Smrekar and Kiefer 1997), do not host ribbon structures. So if volcanic rises and highland plateaus each result from mantle upwelling, the differences between these tectonic features might be attributed to lithosphere thickness.

Differences in lithosphere thickness could be either spatial or temporal. If spatial, we would expect to see young highland plateaus, but we do not. All highland plateaus have crater densities greater than or similar to the mean crater density (Gilmore *et al.* 1997). In addition, highland plateaus are isostatically compensated by thickened crust (e.g., Grimm 1994, Simons *et al.* 1997), rather than thermally compensated as would be expected if some of them were young. Therefore, the difference in lithosphere thickness for highland plateaus and volcanic rises is likely temporal.

Volcanic rises and highland plateaus are similar in planform shape and size, but they differ in topographic profile, gravity signature, and surface geology (e.g., Phillips and Hansen 1994, Hansen *et al.* 1997). Volcanic rises' large gravity anomalies with large depth of apparent compensation (e.g., Smerkar and Phillips 1991, Grimm and Phillips 1992) provide evidence of their relative youth, an interpretation supported by crater densities (Price and Suppe 1994, Phillips and Izenberg 1995, Price *et al.* 1996). In contrast, highland plateaus display small gravity anomalies with shallow depths of compensation, indicating thick crustal roots and lacking any evidence of current thermal support (e.g., Bindschadler *et al.* 1992b, Grimm 1994, Herrick 1994, Simons *et al.* 1997). Highland plateaus are likely ancient features, given that they, on average, display crater densities similar to the planetary average, which is probably a retention age rather than a production age based on the presence of ribbon structures. The available data are consistent with highland plateaus as *ancient* features, representing the surface expression of mantle plumes on a thin lithosphere, whereas volcanic rises represent the *contemporary* surface signature of mantle plumes on a thick lithosphere (Hansen *et al.* 1996; Phillips and Hansen 1997a, 1997b). Phoebe Regio, characterized by a complex pattern of extensional graben, would have formed during a time of intermediate lithosphere thickness.

SUMMARY

In summary, ribbon structures characterize highland plateau deformation, and the nature of ribbon deformation is important to understanding the mode of highland plateau formation. Any model of ribbon formation must account for the following constraints on ribbon geometry. (a) Ribbon-forming lineaments exhibit sharp contrasts relative to adjacent materials. (b) Ribbon-bounding lineaments form a distinct pattern alternating between radar-dark and radar-bright, which represent trough walls oriented away from and toward the satellite, respectively. (c) Ribbons form long, narrow troughs that alternate with parallel, narrow ridges; ridges and trough display extreme length : width aspect ratios. (d) Trough walls are near-vertical. (e) Troughs are shallow with consistent shallow depth along individual troughs and in adjacent troughs. (f) In some cases (e.g., southwest Fortuna Tessera) opposite trough walls are parallel and matched and would exhibit a close fit if the troughs were closed; in these cases trough walls merge laterally forming V-shaped terminations. Trough floors are smooth and flat, lacking small-scale interior lineaments. (g) In other cases (e.g., Thetis Regio) ribbons display (a)–(d), but trough walls are defined by a series of subparallel lineaments including local interior lineaments, and trough floors ramp up to join trough walls displaying parallel rather than V-shaped terminations. Trough walls would not display a close fit if closed.

Tensile-fracture ribbons display features (a)–(f) and formed by the opening of tensile fractures of a thin brittle layer above a ductile substrate. They require a near fracture-free shallow crust and very shallow depth to BDT ($<$1 km). Shear-fracture ribbons display features (a)–(d) and (g) formed under near-surface transitional-tensile failure conditions or due to reactivation of steeply oriented preexisting fractures resulting in steep-sided graben. Formation of tensile-fracture ribbons would be favored with a sharp BDT at very shallow depth, whereas a broader and somewhat deeper BDT would favor formation of shear-fracture ribbons. In both cases, the thickness of the strong upper layer is quite thin ($<$1–2 km), and ribbon structures likely formed prior to long-wavelength folds which require a greater effective elastic thickness and a deeper depth of support ($\sim$6 km).

The widespread presence of ribbon structures within highland plateaus favors an upwelling model for highland plateau formation, in which crustal thickening results from magmatic underplating related to a mantle upwelling or mantle plume. In order for the plume to be able to anneal mechanically the crust as required by ribbon formation, the lithosphere would likely have to be quite thin. These implications are consistent with highland plateaus as an ancient signature of mantle plumes on thin lithosphere. Thermal and rheological constraints imposed by ribbon structures on models of highland plateaus formation (which form the topic of future and concurrent research as they are outside the limits of the present contribution) will provide tests of this hypothesis, as will further detailed structural mapping of highland plateaus with attention to spatial and temporal relations of structural elements.

ACKNOWLEDGMENTS

This work was supported by National Aeronautics and Space Administration Grant NAGW-2915 to VLH. Discussions with Heather DeShon, Becky Ghent, Doug Oliver, Roger Phillips, and Matthew Pritchard were extremely helpful. Critical reviews by Matt Golombek and George McGill greatly improved the manuscript.

REFERENCES

Anderson, E. M. 1951. *The Dynamics of Faulting*, Oliver and Boyd, Edinburg, Scotland.

Baldwin, R. B. 1971. Rima Golcenius II. *J. Geophys. Res.* **76,** 8459–8465.

Barsukov, V. L., and 11 colleagues 1985. Main types of structures of the northern hemisphere of Venus. *Solar System Res.* **19,** 1–9.

Barsukov, V. L., and 29 colleagues 1986. The geology and geomorphology of the Venus surface as revealed by the radar images obtained by Veneras 15 and 16. *J. Geophys. Res.* **91,** D378–D398.

Basilevsky, A. T., A. A. Pronin, L. B. Ronca, V. P. Kryuchkov, A. L. Sukhanov, and M. S. Markov 1986. Styles of tectonic deformations on Venus: Analysis of Venera 15 and 16 data. *J. Geophys. Res.* **91,** D399–D411.

Bindschadler, D. L., and J. W. Head 1991. Tessera terrain, Venus: Characterization and models for origin and evolution. *J. Geophys. Res.* **96,** 5889–5907.

Bindschadler, D. L., M. A. Krevlavsky, M. A. Ivanov, J. W. Head, A. T. Basilevsky, and Y. G. Shkuratov 1990. Distribution of tessera terrain on Venus: Prediction for Magellan. *Geophys. Res. Lett.* **17,** 171–174.

Bindschadler, D. L., A. deCharon, K. K. Beratan, S. E. Smrekar, and J. W. Head 1992a. Magellan observations of Alpha Regio: Implications for formation of complex ridged terrains on Venus. *J. Geophys. Res.* **97,** 13,563–13,577.

Bindschadler, D. L., G. Schubert, and W. M. Kaula 1992b. Coldspots and hotspots: Global tectonics and mantle dynamic of Venus. *J. Geophys. Res.* **97,** 13,495–13,532.

Brace, W. F. 1960. An extension of the Griffith theory of fracture to rocks. *J. Geophys. Res.* **65,** 3477–3480.

Brown, C. D., and R. E. Grimm 1996. Lithospheric rheology and flexure at Artemis Chasma, Venus. *J. Geophys. Res.* **101,** 12,697–12,708.

Brown, C. D., and R. E. Grimm 1997. Tessera deformation and the contemporaneous thermal state of the plateau highlands, Venus. *Earth Planet. Sci. Lett.* **147,** 1–10.

Connors, C. 1995. Determining heights and slopes of fault scarps and other surfaces on Venus using Magellan stereo radar. *J. Geophys. Res.* **100,** 14,361–14,381.

Ekström, T. K. 1975. Pinch-and-swell structures from a Swedish locality. *Geol. Foren. Stockholm. Forh.* **97,** 180–187.

Ford, J. P., J. J. Plaut, C. M. Weitz, T. G. Farr, D. A. Senske, E. R. Stofan, G. Michaels, and T. J. Parker 1993. *Guide to Magellan Image Interpretation*, JPL Publication 93(24).

Ghent, R. R., and V. L. Hansen 1997. Structural analysis of central and eastern Ovda Regio, Venus. *Lunar Planet. Sci.* **XXVIII,** 409–410.

Ghosh, S. K. 1988. Theory of chocolate tablet boudinage. *J. Geophys. Res.* **10,** 541–553.

Gilmore, M. S., Ivanov, M. I., J. W. Head, and A. T. Basilevsky 1997. Duration of tessera deformation on Venus. *J. Geophys. Res.* **102,** 13,357–13,368.

Golombek, M. P. 1979. Structural analysis of lunar grabens and the shallow crustal structure of the moon. *J. Geophys. Res.* **84,** 4657–4666.

Golombek, M. P., and W. B. Banerdt 1986. Early thermal profiles and lithospheric strength of Ganymede from extensional tectonic features. *Icarus* **68,** 252–265.

Golombek, M. P., and W. B. Banerdt 1990. Constraints on the subsurface structure of Europa. *Icarus* **83,** 441–452.

Grimm, R. E. 1994. The deep structure of venusian plateau highlands. *Icarus* **112,** 89–103.

Grimm, R. E., and R. J. Phillips 1992. Anatomy of a venusian hot spot: Geology, gravity, and mantle dynamics of Eistla Regio. *J. Geophys. Res.* **97,** 16,035–16,054.

Grimm, R. E., and S. C. Solomon 1988. Viscous relaxation of impact crater relief on Venus: Constraints on crustal thickness and thermal gradient. *J. Geophys. Res.* **93,** 11,911–11,929.

Hansen, V. L., and J. J. Willis 1996. Structural analysis of a sampling of tesserae: Implications for Venus geodynamics. *Icarus* **123,** 296–312.

Hansen, V. L., J. J. Willis, and R. J. Phillips 1996. Structural evolution of crustal plateaus, Venus (abstract). *Eos* **77**(22), 83.

Hansen, V. L., J. J. Willis, and W. B. Banerdt 1997. Tectonic overview and synthesis. In *Venus II* (S. W. Bougher, D. M. Hunten, and R. J. Phillips, Eds.), pp. 797–844. Arizona Univ. Press, Tucson.

Herrick, R. R. 1994. Resurfacing history of Venus. *Geology* **22,** 703–706.

Herrick, R. R., B. G. Bills, and S. A. Hall 1989. Variations in effective compensation depth across Aphrodite Terra, Venus. *Geophys. Res. Lett.* **16,** 543–546.

Herrick, R. R., and R. J. Phillips 1990. Blob tectonics: A prediction for western Aphrodite Terra, Venus. *Geophys. Res. Lett.* **17,** 2129–2132.

Hubbert, M. K., and W. Rubey 1959. Role of fluid pressure in mechanics of overthrust faulting, Pts. I and II. *Geol. Soc. Am. Bull.* **70,** 115–205.

Ivanov, M. A., and A. T. Basilevsky 1993. Density and morphology of impact craters on tessera terrain, Venus. *Geophys. Res. Lett.* **20,** 2579–2582.

Jaeger, J. C., and N. G. W. Cook 1979. *Fundamentals of Rock Mechanics*, 3rd ed., Chapman and Hall, London.

Kaula, W. M. 1990. Venus: A contrast in evolution to Earth. *Science* **247,** 1191–1196.

Kidan, T. W., and J. W. Cosgrove 1996. The deformation of multilayers by layer-normal compression: An experimental investigation. *J. Struc. Geol.* **18,** 461.

Lloyd, G. E., C. C. Ferguson, and K. Reading 1982. A stress transfer model for the development of extension fracture boudinage. *J. Struc. Geol.* **4,** 355–372.

Lohest, M. 1909. De l'origine des veines et des géodes des terrains de Belgique. *Soc. Géol. Belgique Annales* **36B,** 275–282.

Mankin, J. H. 1950. The down-structure method of viewing geologic maps. *J. Geol.* **58,** 55–72.

McGill, G. E. 1971. Attitude of fractures bounding straight and arcuate lunar rilles. *Icarus* **14,** 53–58.

McGill, G. E., and A. W. Stromquist 1979. The grabens of Canyonlands National Park, Utah: Geometry, mechanics and kinematics. *J. Geophys. Res.* **84,** 4547–4563.

Moore, J. M. 1997. Displacement-length scaling, kinematics and mechanical implications of Canyonlands National Park grabens. MS thesis, Univ. of Nevada, Reno.

Moore, J. M., and R. A. Schultz 1996. Mechanisms for graben growth: Evidence from fossil and active relay-ramps at Canyonlands National Park. *Eos* **77**(23), F643. [Abstract]

Moore, J. M., R. A. Schultz, E. B. Grosfils, A. N. Fori, W. H. Roadarmel, N. I. Bush, C. Harris, and C. B. Ivers 1997. The 1996 Canyonlands initiative: Field study of small planetary grabens. *Lunar Planet. Sci.* **XXVIII,** 975–976.

Phillips, R. J., and V. L. Hansen 1994. Tectonic and magmatic evolution of Venus. *Annu. Rev. Earth Planet. Sci.* **22,** 597–654.

Phillips, R. J., and V. L. Hansen 1997. Venus now and then. *Lunar Planet. Sci.* **XXVIII,** 1105–1106.

Phillips, R. J., and V. L. Hansen 1997. Geological evolution of Venus rises, plains, plumes, and plateaus. *Science* **279,** 1492–1497.

Phillips, R. J., and N. R. Izenberg 1995. Ejecta correlations with spatial crater density and Venus resurfacing history. *Geophys. Res. Lett.* **22,** 1517–1520.

Phillips, R. J., R. E. Grimm, and M. C. Malin 1991. Hot-spot evolution and the global tectonics of Venus. *Science* **252,** 651–658.

Phillips, R. J., C. L. Johnson, S. J. Mackwell, P. Morgan, D. T. Sandwell,

and M. T. Zuber 1997. Lithospheric mechanics and dynamics of Venus. In *Venus II* (S. W. Bougher, D. M. Hunten, and R. J. Phillips, Eds.), pp. 149–214. Arizona Univ. Press, Tucson.

Plaut, J. J. 1993a. *Stereo Imaging*, JPL Publication 93(24), pp. 33–41.

Plaut, J. J. 1993b. *The Non-SAR Experiments*, JPL Publication 93(24), pp. 19–31.

Pollard, D. D., and A. Aydin 1988. Progress in understanding jointing over the past century. *Geol. Soc. Am. Bull.* **100,** 1181–1204.

Price, N. J., and J. W. Cosgrove 1990. *Analysis of Geological Structures*, Cambridge Univ. Press, Cambridge, England.

Price, M., and J. Suppe 1994. Mean age of rifting and volcanism on Venus deduced from impact crater densities. *Nature* **372,** 756–759.

Price, M. H., G. Watson, and C. Brankman 1996. Dating volcanism and rifting on Venus using impact crater densities. *J. Geophys. Res.* **101,** 4657–4671.

Pritchard, M. E., V. L. Hansen, and J. J. Willis 1997. Structural evolution of western Fortuna Tessera, Venus. *Geophys. Res. Lett.* **24,** 2339–2342.

Ramberg, H. 1955. Natural and experimental boudinage and pinch-and-swell structures. *J. Geol.* **63,** 512–526.

Ryan, M. P., and C. G. Sammis 1981. The glass transition in basalt. *J. Geophys. Res.* **86,** 9519–9535.

Schultz, R. A. 1993. Brittle strength of basaltic rock masses with applications to Venus. *J. Geophys. Res.* **98,** 10,833–10,895.

Sibson, R. H. 1985. A note on fault reactivation. *J. Struc. Geol.* **7,** 751–754.

Simons, M., B. H. Hager, and S. C. Solomon 1994. Global variations in the geoid/topography admittance of Venus. *Science* **264,** 798–803.

Simons, M., S. C. Solomon, and B. H. Hager 1997. Localization of gravity and topography: Constraints on the tectonics and mantle dynamics of Venus. *Geophys. J. Int.* **131,** 24–31.

Smith, R. B. 1975. Unified theory of the onset of folding, boudinage and mullion structure. *Geol. Soc. Am. Bull.* **86,** 1601–1609.

Smith, R. B. 1977. Formation of folds, boudinage and mullions in non-Newtonian materials. *Geol. Soc. Am. Bull.* **88,** 312–320.

Smith, R. B. 1979. The folding of a strongly non-Newtonian layer. *Am. J. Sci.* **279,** 272–287.

Smrekar, S. E., and R. J. Phillips 1991. Venusian highlands: Geoid to topography ratios and their implications. *Earth Planet. Sci. Lett.* **107,** 582–597.

Smrekar, S. E., and W. S. Kiefer 1997. Large volcanic rises. In *Venus II* (S. W. Bougher, D. M. Hunten, and R. J. Phillips, Eds.), pp. 845–878. Arizona Univ. Press, Tucson.

Solomon, S. C., J. W. Head, W. M. Kaula, D. McKenzie, B. Parsons, R. J. Phillips, G. Schubert, and M. Talwani 1991. Venus tectonics: Initial analysis from Magellan. *Science* **252,** 297–312.

Solomon, S. C., S. E. Smrekar, D. L. Bindschadler, R. E. Grimm, W. M. Kaula, G. E. McGill, R. J. Phillips, R. S. Saunders, G. Schubert, S. W. Squyres, and E. R. Stofan 1992. Venus tectonics: An overview of Magellan observations. *J. Geophys. Res.* **97,** 13,199–13,255.

Stromgard, K. E. 1973. Stress distribution during formation of boudinage and pressure shadows. *Tectonophys.* **16,** 215–248.

Sukhanov, A. L. 1986. Parquet: Regions of areal plastic dislocations. *Geotectonics* **20,** 294–305.

Sukhanov, A. L. 1987. Parquet on Venus: Areas of regional deformations. *Lunar Planet. Sci.* **XVIII,** 972–973.

Suppe, J., and C. Connors 1992. Critical taper wedge mechanics of fold-thrust-belts on Venus: Initial result from Magellan. *J. Geophys. Res.* **97,** 13,545–13,562.

Talbot, C. J. 1970. The minimum strain ellipsoid using deformed quartz veins. *Tectonophys.* **9,** 47–76.

Tanaka, K. L., and M. P. Golombek 1989. Martian tension fractures and the formation of grabens and collapse features at Valles Marineris. *Proc. Lunar Planet. Sci. Conf.* **19**, 383–396.

Trudgill, B., and J. Cartwright 1994. Relay-ramp forms and normal-fault linkages, Canyonlands National Park, Utah. *Geol. Soc. Am. Bull.* **106,** 1143–1157.

Twiss, R. J., and E. M. Moores 1992. *Structural Geology*, Freeman, New York.

Weitz, C. M. 1993. *Impact craters*. JPL Publication 93(24), pp. 75–92.

Willis, J. J. 1997. Using single-cycle Magellan radar imagery to constrain heights and slope angles of venusian geologic features. *Lunar Planet. Sci.* **XXVIII,** 1561–1562.

Zuber, M. T. 1987. Constraints on the lithospheric structure of Venus from mechanical models and tectonic surface features. *J. Geophys. Res.* 92, E541-E551.